

Spectroscopic and Theoretical Studies of Mononuclear Copper(II) Alkyl- and Hydroperoxo Complexes: Electronic Structure Contributions to Reactivity

Peng Chen,[†] Kiyoshi Fujisawa,^{*,‡} and Edward I. Solomon^{*,†}

Contribution from the Departments of Chemistry, Stanford University, Stanford, California, 94305, and University of Tsukuba, Tsukuba, 305-8571, Japan

Received May 15, 2000. Revised Manuscript Received August 10, 2000

Abstract: Spectroscopic studies combined with calculations are used to describe the electronic structure and vibrational properties of mononuclear four-coordinate end-on alkylperoxo and hydroperoxo Cu(II) complexes. EPR defines a Cu x^2-y^2 ground state with $\sim 62\%$ Cu character. From absorption, MCD, and resonance Raman spectroscopies, the main bonding interaction between the alkyl(hydro)peroxide and Cu(II) is found to involve the π -donation of the alkyl(hydro)peroxide π^*_v into the Cu x^2-y^2 orbital, which dominates the observed spectroscopic features, producing an intense absorption band at $\sim 16\,600\text{ cm}^{-1}$ ($\sim 600\text{ nm}$). On the basis of the vibrational frequencies, isotope shifts, and normal coordinate analyses, the dominant vibrations of the alkyl-(hydro)peroxo complexes are assigned and the Cu–O and O–O force constants are determined. The observed strong Cu–O bond and the large alkyl(hydro)peroxide-to-Cu(II) charge donation are ascribed to the low coordination number of Cu and the distorted T_d ligand field. The observed strong O–O bond mainly derives from polarization by the alkylcarbon/proton. The unoccupied peroxide σ^* orbital is also greatly stabilized in energy, and the complexes are activated for electrophilic attack. Experimentally calibrated density functional calculations, coupled with frontier molecular orbital theory, are employed to obtain insight into the reactivity of these model complexes. Mechanisms of electrophilic attack, O–O bond cleavage, and H atom abstraction are evaluated, and their relevance to dopamine β -monooxygenase and peptidylglycine α -hydroxylating monooxygenase reactivities is considered.

Introduction

Oxygen binding, activation, and reduction are often carried out by copper enzymes.^{1,2} These enzymes exhibit unique spectroscopic features which reflect novel electronic structures that can make key contributions to reactivity. The binuclear copper enzymes can be divided into two classes with coupled or noncoupled³ active sites, where the coupled sites have electronic interactions between the two coppers (e.g., antiferromagnetic exchange or dipolar coupling). Electronic coupling can allow the two coppers to act concertedly in multielectron redox reactivity.

The coupled binuclear copper proteins, hemocyanin, tyrosinase, catechol oxidase, and related model complexes are the most well studied in terms of electronic structure/function correlations.^{4,5} These have two Cu(II) centers bridged by a side-on ($\mu\text{-}\eta^2\text{:}\eta^2$) peroxide (Cu–Cu $\approx 3.6\text{ \AA}$) and exhibit no EPR signal due to the strong antiferromagnetic exchange coupling associated with the peroxide bridge. The two HOMO valence orbitals of the peroxide, π^*_{σ} and π^*_v (π^*_{σ} is the peroxide antibonding π^* orbital located in the Cu₂O₂ plane and π^*_v is perpendicular

to the plane), dominate the bonding, where the π^*_{σ} orbital is involved in two σ -donor bonds to each of the two coppers. There is additional back-bonding from the two coppers into the σ^* LUMO of the peroxide, which thus acts as a π acceptor ligand. These bonding interactions produce unique spectroscopic features. The strong σ -donor bond produces an intense π^*_{σ} -to-Cu(II) charge-transfer (CT) absorption band, and the back-bonding into the peroxide σ^* orbital results in a very low O–O stretching frequency, which reflects an extremely weak O–O bond activated for cleavage.^{6,7} In contrast, far less is known about geometric and electronic structure/function correlations for the noncoupled binuclear copper enzymes, dopamine β -monooxygenase (D β M) and peptidylglycine α -hydroxylating monooxygenase (PHM), where, in principle, a peroxide intermediate may be activated by coordination to only one copper ion (vide infra).¹

D β M catalyzes the conversion of dopamine to norepinephrine by inserting an oxygen atom from dioxygen into the benzylic position of the ethylamine side chain of dopamine.^{8,9} Two of the electrons required in this process come from the substrate, and the other two are supplied by the exogenous electron donor ascorbic acid. Although the crystal structure of D β M is not known, studies have shown that the protein contains two noncoupled copper ions per subunit ($>7\text{ \AA}$ apart by EPR).¹⁰

[†] Stanford University.

[‡] University of Tsukuba.

(1) Klinman, J. P. *Chem. Rev.* **1996**, *96*, 2541.

(2) Solomon, E. I.; Sundaram, U. M.; Machonkin, T. E. *Chem. Rev.* **1996**, *96*, 2563.

(3) Noncoupled binuclear: two copper sites with no electronic interaction (dipolar or exchange) between them.

(4) Solomon, E. I.; Baldwin, M. J.; Lowery, M. D. *Chem. Rev.* **1992**, *92*, 521.

(5) Solomon, E. I.; Tuzek, F.; Root, D. E.; Brown, C. A. *Chem. Rev.* **1994**, *94*, 827.

(6) Ross, P. K.; Solomon, E. I. *J. Am. Chem. Soc.* **1991**, *113*, 3246.

(7) Baldwin, M. J.; Root, D. E.; Pate, J. E.; Fujisawa, K.; Kitajima, N.; Solomon, E. I. *J. Am. Chem. Soc.* **1992**, *114*, 10421.

(8) Winkler, H.; Apps, D. K.; Fischer-Colbrie, R. *Neuroscience* **1986**, *18*, 261.

(9) Stewart, L. C.; Klinman, J. P. *Annu. Rev. Biochem.* **1988**, *57*, 551.

Biochemical studies have strongly suggested that the two Cu sites are inequivalent with the Cu_A site involved in electron transfer to Cu_B and the Cu_B site catalyzing oxygen insertion.¹¹ The coordination geometries of the copper sites have been studied extensively by EXAFS and edge absorption. The Cu_B site has two coordinated histidines (Cu–N = 1.99 ± 0.03 Å), a S-donor ligand (generally believed to be a methionine, Cu–S = 2.25 ± 0.02 Å), and a fourth ligand X (Cu–X = 2.53 ± 0.03 Å).¹² Three-histidine ligation is inferred for the Cu_A site from the EXAFS averaged ligand environment.¹³

The DβM reaction has been studied mainly by steady-state kinetics. A mononuclear Cu(II) hydroperoxo intermediate (Cu^{II}OOH) at the Cu_B site has been proposed as the activated dioxygen species, which is thought to perform a H atom abstraction reaction. Although recent ¹⁸O isotope labeling studies argue that O–O bond cleavage occurs prior to C–H bond cleavage by attack on a protein side chain and the resulting Cu^{II}–oxyl/Cu^{III}–oxo species attacks the substrate, a mononuclear Cu^{II}OOH intermediate is generally believed to be the active oxygen species in this reaction.¹⁴

PHM, which catalyzes the stereospecific hydroxylation of the glycine α-carbon of peptidylglycine substrates, is mechanistically very similar to DβM.^{15–20} The crystal structure of the rat PHM catalytic core (PHMcc) has been recently solved for both the reduced and oxidized sites.^{21,22} The crystallographic studies on the oxidized form of PHMcc have shown that it is composed of two domains. Domain 1 binds one copper (Cu_A) with three histidine Nδ ligands, while domain 2 binds the other copper (Cu_B) with two histidine Nε ligands, a methionine sulfur, and a solvent molecule (water) displaying a distorted tetrahedral site symmetry. The Cu_A and Cu_B sites are 11 Å apart, separated by a solvent-filled interdomain cleft. The Cu ligation environment of the reduced form of PHMcc is very similar to the oxidized form with minor differences in ligand distances and angles. Although mechanistic studies of the hydroxylation reaction of PHM are not as extensive as those for DβM, the oxygenation reaction pathway is generally proposed to parallel the DβM reaction, and a similar mononuclear hydroperoxo intermediate Cu^{II}OOH is believed to be involved in catalysis.¹ The nature of this mononuclear Cu(II) hydroperoxo intermediate and its activation for the O–O cleavage step of H atom abstraction are not understood.

Studies of inorganic model systems have greatly contributed to the understanding of biological systems, and much effort has been devoted to the design and synthesis of inorganic models of the catalytic sites of DβM and PHM.^{23–27} A five-coordinate, μ-1,1-bridged binuclear Cu(II) acylperoxo complex, Cu₂OOR

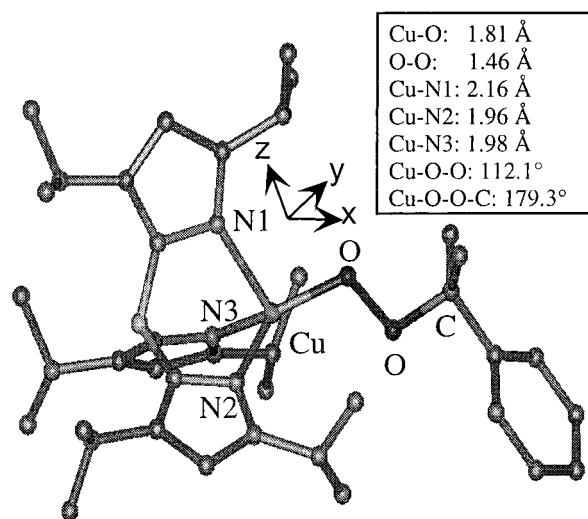


Figure 1. Crystal structure of Cu(OOCMe₂Ph)(HB(3,5-Pr₂Pz)₃) (L1CuOOcm).

(R = *m*-ClC₆H₄C(O)–), has been structurally defined to have $r(\text{Cu–O}) = 1.96 \text{ Å}$, $r(\text{O–O}) = 1.46 \text{ Å}$, and $\theta(\text{Cu–O–O}) = 123^\circ$.²⁸ Spectroscopic studies on a series of related complexes with different Cu ligand systems, as well as a hydroperoxo complex (Cu₂OOH),^{29,30} demonstrate that the peroxide dominates the metal–ligand bonding and gives rise to an intense CT band at $\sim 25\,300 \text{ cm}^{-1}$ ($\epsilon \approx 6000 \text{ M}^{-1} \text{ cm}^{-1}$). The O–O bond in the Cu₂OOH complex is activated for electrophilic attack due to protonation of the peroxide, and the hydroperoxo ligand is a rather poor donor to the Cu(II) center.³⁰ Recently, a mononuclear Cu(II) alkylperoxo complex, Cu(OOCMe₂Ph)(HB(3,5-Pr₂pz)₃), has been synthesized and structurally characterized. It shows spectroscopic features strikingly different from those of Cu₂OOR(H), with a low-energy intense absorption band centered at $\sim 17\,700 \text{ cm}^{-1}$.²⁶ The molecule has a four-coordinate distorted tetrahedral environment comprised of a trispyrazolylborate ligand system and an alkylperoxide (Figure 1). The O–O distance of 1.46 Å is in the range of those reported for other alkylperoxo transition metal complexes. In contrast to the μ-1,1-bridged five-coordinate species, the Cu–O bond of this four-coordinate complex is very short, 1.81 vs 1.96 Å for Cu₂OOR. The three nitrogen atoms of the trispyrazolylborate ligand bind inequivalently to the Cu, with one elongated axial Cu–N bond (2.16 Å) and two short equatorial Cu–N bonds (1.98 and 1.96 Å, respectively). This leads to an approximately trigonally distorted *T_d* site with the C₃ being the long axis. With the Cu–O–O angle of 112.1° and Cu–O–O–C dihedral angle at almost 180° (i.e., 179.3°), the molecule has an approximate C_s core structure, with the mirror plane containing the long axial Cu–N and the Cu–O bonds.

In this study, we extend our spectroscopic and electronic structure studies of Cu/O₂ model complexes to the mononuclear

(10) Ljones, T.; Skotland, T. In *Copper Proteins and Copper Enzymes*; Lontie, R., Ed.; CRC Press: Boca Raton, 1984; p 131.

(11) Brenner, M. C.; Kliman, J. P. *Biochemistry* **1989**, *28*, 4664.

(12) Reedy, B. J.; Blackburn, N. J. *J. Am. Chem. Soc.* **1994**, *116*, 1924.

(13) Blackburn, N. J.; Hasnain, S. S.; Pettingill, T. M.; Strange, R. W. *J. Biol. Chem.* **1991**, *266*, 23120–23127.

(14) Tian, G.; Berry, J. A.; Klinman, J. P. *Biochemistry* **1994**, *33*, 226.

(15) Eipper, B. A.; Stoffers, D. A.; Mains, R. E. *Annu. Rev. Neurosci.* **1992**, *15*, 57.

(16) Eipper, B. A.; Milgram, S. L.; Husten, E. J.; Yun, H.-Y.; Mains, R. E. *Protein Sci.* **1993**, *2*, 489.

(17) Katopodis, A. G.; May, S. W. *Biochemistry* **1990**, *29*, 4541.

(18) Merkler, D. J. *Enzyme Microb. Technol.* **1994**, *16*, 450.

(19) Suzuki, K.; Ohta, M.; Okamoto, M.; Nishikawa, Y. *Eur. J. Biochem.* **1993**, *213*, 93.

(20) Bradbury, A. F.; Smyth, D. G. *Trends Biochem. Sci.* **1991**, *16*, 112.

(21) Prigge, S. T.; Kolhekar, A. S.; Eipper, B. A.; Mains, R. E.; Amzel, L. M. *Science* **1997**, *278*, 1300.

(22) Prigge, S. T.; Kolhekar, A. S.; Eipper, B. A.; Mains, R. E.; Amzel, L. M. *Nat. Struct. Biol.* **1999**, *6*, 976.

(23) Champloy, F.; Benali-Chérif, N.; Bruno, P.; Blain, I.; Pierrot, M.; Réglier, M.; Michalowicz, A. *Inorg. Chem.* **1998**, *37*, 3910.

(24) Wada, A.; Harata, M.; Hasegawa, K.; Jitsukawa, K.; Masuda, H.; Mukai, M.; Kitagawa, T.; Einaga, H. *Angew. Chem., Int. Ed. Engl.* **1998**, *37*, 798.

(25) Sanyal, I.; Ghosh, P.; Karlin, K. D. *Inorg. Chem.* **1995**, *34*, 3050.

(26) Kitajima, N.; Katayama, T.; Fujisawa, K.; Iwata, Y.; Moro-oka, Y. *J. Am. Chem. Soc.* **1993**, *115*, 7872.

(27) Kitajima, N.; Fujisawa, K.; Moro-oka, Y. *Inorg. Chem.* **1990**, *29*, 357.

(28) Ghosh, P.; Tyeklar, Z.; Karlin, K. D.; Jacobson, R. R.; Zubiata, J. *J. Am. Chem. Soc.* **1987**, *109*, 6889.

(29) Karlin, K. D.; Ghosh, P.; Cruse, R. W.; Farooq, A.; Gultneh, Y.; Jacobson, R. R.; Blackburn, N. J.; Strange, R. W.; Zubiata, J. *J. Am. Chem. Soc.* **1988**, *110*, 6769.

(30) Root, D. E.; Mahroof-Tahir, M.; Karlin, K. D.; Solomon, E. I. *Inorg. Chem.* **1998**, *37*, 4838.

Cu(II) alkylperoxo complexes and the corresponding hydroperoxo complex, which serve as models for the proposed but unobserved catalytic intermediate in the D β M and PHM reactions. These studies employ EPR, low-temperature absorption, magnetic circular dichroism (MCD), and resonance Raman (rR) spectroscopies and are complemented by density functional theory (DFT) and semiempirical INDO/S-CI molecular orbital (MO) calculations. The electronic and vibrational properties are analyzed, and the theoretical electronic structure calculations of Cu(II)-alkyl(hydro)peroxo bonding are evaluated. Results are compared to those obtained for the five-coordinate Cu₂OOH model and are extended to obtain insight into the reactivity of these model complexes. The electrophilic attack, O–O bond cleavage, and H atom abstraction reactions of the alkyl(hydro)peroxo Cu(II) intermediate are evaluated, and their relevance to D β M and PHM reactivities is considered.

Experimental Section

Materials. All reagents were of the highest grade commercially available and were used without further purification. Alkylperoxo complexes, Cu(OOCMe₂Ph)(HB(3,5-^tPrpz)₃), Cu(OOCMe₂Ph)(HB(3-^tBu-5-^tPrpz)₃), and Cu(OOtBu)(HB(3-^tBu-5-^tPrpz)₃ (referred to as L1CuOOCm, L3CuOOCm, L3CuOOtBu, respectively), were synthesized as previous reported.²⁶ The hydroperoxo complex, Cu(OOH)(HB(3-^tBu-5-^tPrpz)₃ (referred to as L3CuOOH), was synthesized in a one-step reaction from starting material Cu(OH)(HB(3-^tBu-5-^tPrpz)₃ (referred to as L3CuOH).³¹ An 18-mg sample of L3CuOH was dissolved in 3 mL of degassed *tert*-butylbenzene, and at –50 °C (dry ice/MeCN), 18 μ L of 30% H₂O₂ was added. The reaction is complete in about an hour.

Spectroscopic Studies. EPR spectra were recorded at liquid nitrogen temperature on a Bruker 220-D SRC spectrometer in a finger dewar. Low-temperature absorption spectra were measured on a double-beam spectrophotometer (Cary 17 and Cary 500) using a liquid helium cryostat (Janis Research Super Vari-Temp). MCD data were collected on CD spectropolarimeters (JASCO J500/J810 with S20 PM tubes for the UV/vis regions, and JASCO J200 with InSb detector for the near-IR region) with sample compartments modified to accommodate magnetocryostats (Oxford Instruments, SM4–7T). Mulls were prepared by grinding the solid material in a mortar embedded in dry ice in a glovebag purged with nitrogen gas. The fine powder was suspended in mineral oil and spread between precooled quartz disks.

Raman spectra were obtained using a series of lines of Kr⁺ (Coherent 190C-K) and Ar⁺ (Coherent Sabre 25/7) ion lasers with incident power in the 5–25 mW range using an \sim 135° backscattering arrangement. The scattered light was dispersed by a triple monochromator (Spex 1877 CP, equipped with 1200, 1800, and 2400 grooves/mm gratings) and detected with a back-illuminated CCD camera (Princeton Instruments ST-135). The samples in NMR tubes were immersed in liquid nitrogen using an EPR finger dewar. Profiles were obtained by measuring the Raman spectra of 3–5 samples, first with excitation at 568.2 nm to scale the intensity, and then at the wavelength of interest, and subsequently back to 568.2 nm to monitor the sample integrity. Background spectra of pure solid Na₂SO₄ (for solid samples) and pure solvent (for solution samples) were taken under the same conditions. Background spectra of charcoal in the same NMR tubes were subtracted to remove the Raman scattering of the quartz sample tube from the data. Peak intensities were determined relative to the 990 cm^{–1} band of Na₂SO₄ for the solid samples and the \sim 700 cm^{–1} band of *tert*-butylbenzene for solution samples. The sample self-absorption was corrected using the Shriver and Dunn formula³² for the high absorbing limit:

$$\frac{\alpha_s}{\alpha_r} = \frac{I_s c_r (\epsilon_s + \epsilon_0)}{I_r c_s (\epsilon_r + \epsilon_0)} \quad (1)$$

(31) Fujisawa, K.; Kobayashi, T.; Fujita, K.; Kitajima, N.; Moro-oka, Y.; Miyashita, Y.; Yamada, Y.; Okamoto, K. *Bull. Chem. Soc. Jpn.* **2000**, 73, 1797.

(32) Shriver, D. F.; Dunn, J. B. R. *Appl. Spectrosc.* **1974**, 28, 319.

where α_s and α_r are the actual intensities and I_s and I_r the measured intensities of sample and reference Raman peaks, respectively. c_s and c_r are the concentrations of sample and reference. ϵ_s , ϵ_r , and ϵ_0 are the extinction coefficients of the absorbing sample at the sample Raman peak, reference Raman peak, and incident laser light energies.

Normal Coordinate Analysis. Normal coordinate analyses (NCA) were performed using the QCPE computer program 576 by M. R. Perterson and D. F. McIntoch, which involves solution of the secular equation $|\mathbf{FG} - \lambda \mathbf{E}| = 0$ ^{33,34} by the diagonalization procedure of Miyazawa.³⁵ The calculations are based on a general valence force field. Force constants are refined with the nonlinear optimization routine of the simplex algorithm according to Nelder and Mead.³⁶

For quantum-chemistry-assisted NCA of the alkylperoxo complex (vide infra), the side chains of the trispyrazolylborate ligand were truncated and replaced by hydrogen atoms. The benzene ring of the cumylperoxide ligand was substituted by a methyl group. This simplified model was then fully optimized at the B3LYP/LANL2DZ level, and a frequency calculation was performed to obtain the generalized valence force field. All related force constants were then introduced to the NCA model, and the **F** matrix was further simplified by eliminating those nondiagonal force constants which do not affect the modes observed in the resonance Raman spectrum. Most force constants were frozen, and selected force constants were varied within the range of the quantum mechanically calculated values to fit the experimental data and obtain a description of the molecular vibrations.

DFT Calculations. Density functional calculations were performed on an SGI Origin 2000 workstation, using Gaussian 94/98.³⁷ Becke's three-parameter hybrid functional with the correlation functional of Lee, Yang, and Parr (B3LYP) was used for all DFT calculations.³⁸ Two types of basis sets were employed. LanL2DZ basis set (Dunning/Huzinaga full double- ζ (D95)³⁹ basis functions on first row atoms, and Los Alamos effective core potentials plus DZ functions on all other atoms)^{40,41} was used mainly for geometry optimizations and frequency calculations. A general basis set (6-311G* for Cu and 6-31G* for all other atoms) was used primarily for single-point calculations. In the reactivity calculations, all total energies were obtained by energy optimization of the molecule under C_s symmetry at the same level of theory as in the single-point calculations, while keeping the pyrazole ring coordinates frozen. Convergence was reached when the relative change in the density matrix between subsequent iterations was less than 1×10^{-4} for single-point calculations and 1×10^{-8} for geometry optimizations. Wave functions were plotted with the visualization program Molden,⁴² and the force constants in internal coordinates were extracted from the Gaussian output using the program Redong.⁴³

The crystal structure of L1CuOOCm was used as the starting point to model the alkylperoxo Cu(II) complex, Pz₃CuOOCm/Cs. The following modifications were made to simplify the calculations: the side chains of the pyrazolyl rings were replaced by hydrogens; the cumylperoxide ligand was modeled by methylperoxide; and the symmetry was averaged to C_s, with the mirror plane going through the long axial Cu–N bond (Figure 1) and the O–O–CH moiety.

(33) Woodward, L. A. *Introduction to the Theory of Molecular Vibrations and Vibrational Spectroscopy*; Clarendon Press: Oxford, 1972.

(34) Wilson, E. B., Jr.; Decius, J. C.; Cross, P. C. *Molecular Vibrations*; Dover Publications: New York, 1980.

(35) Miyasawa, T. *J. Chem. Phys.* **1958**, 29, 246.

(36) Nelder, J. A.; Mead, R. *Comput. J.* **1965**, 7, 308.

(37) Frisch, M. J.; Trucks, G. W.; Schlegel, H. B.; Gill, P. M. W.; Johnson, B. G.; Robb, M. A.; Cheeseman, J. R.; Keith, T. A.; Peterson, G. A.; Montgomery, J. A.; Raghavachari, K.; Al-Laham, M. A.; Zakrzewski, V. G.; Ortiz, J. V.; Foresman, J. B.; Cioslowski, J.; Stefanov, B. B.; Nanayakkara, A.; Challacombe, M.; Peng, C. Y.; Ayala, P. Y.; Chen, W.; Wong, M. W.; Andres, J. L.; Replogle, E. S.; Gomperts, R.; Martin, R. L.; Fox, D. J.; Binkley, J. S.; Defrees, D. J.; Baker, J.; Stewart, J. P.; Head-Gordon, M.; Gonzalez, C.; Pople, J. A. *Gaussian 94/98*; Gaussian, Inc.: Pittsburgh, 1995.

(38) Becke, A. D. *J. Chem. Phys.* **1993**, 98, 5648.

(39) Dunning, T. H., Jr.; Hay, P. J. In *Modern Theoretical Chemistry*, 3rd ed.; Schaefer, H. F., Ed.; Plenum: New York, 1976.

(40) Hay, P. J.; Wadt, W. R. *J. Chem. Phys.* **1985**, 82, 270 and 299.

(41) Wadt, W. R.; Hay, P. J. *J. Chem. Phys.* **1985**, 82, 284.

(42) Schaftenaar, G.; Noordik, J. H. *J. Comput.-Aided Mol. Des.* **2000**, 14, 123.

(43) Allouche, A. *Spectrochim. Acta* **1993**, 49A, 571.

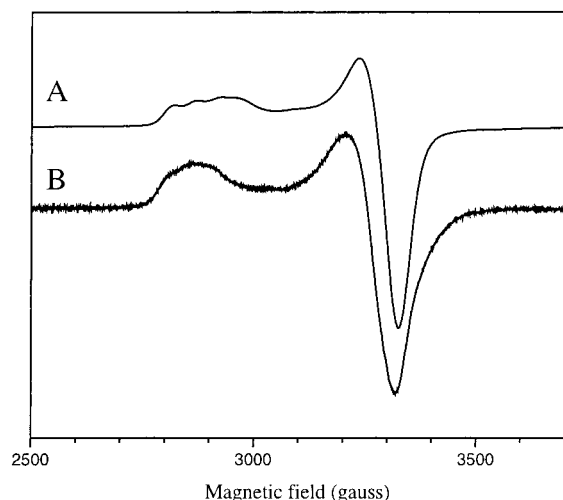


Figure 2. 77 K X-band (9.515 GHz) frozen glass EPR spectra of L3CuOOCm in CH₂Cl₂ (A) and L3CuOOH in toluene (B).

Table 1. Summary of EPR Results of Alkylperoxo and Hydroperoxo Cu(II) Complexes

complex	$g_{ }$	$ A_{ } $ (10^{-4} cm $^{-1}$)	g_{\perp}	$ A_{\perp} $ (10^{-4} cm $^{-1}$)
L3CuOOCm	2.350	56	2.076	
L3CuOOtBu	2.336	57	2.076	
L1CuOOCm	2.316	~55	2.097	<15
L3CuOOH	2.380	~40	2.090	

INDO/S-CI Calculations. Semiempirical calculations were of the valence-only type and carried out with the program Orca, developed by Dr. Frank Neese.⁴⁴ Restricted open-shell (ROHF)⁴⁵ SCF calculations were tightly converged on the ground state, which serves as a reference for configuration interaction (CI) calculations. All single excitations into the singly occupied MOs (SOMOs) and virtual MOs, and from the SOMOs into all virtual orbitals, are included in the CI within the basis set limit. Inclusion of double excitations was not necessary.

rR Profile Simulation. rR excitation profiles were simulated by using the time-dependent theory of electronic spectroscopy developed by Heller and co-workers^{46,47} and a script written for Mathcad 7.0.⁴⁸

Results

EPR. Frozen glass EPR spectra obtained for L3CuOOCm and L3CuOOH are presented in Figure 2. The spectroscopic parameters for alkyl- and hydroperoxo Cu(II) complexes are summarized in Table 1.⁴⁹ L3CuOOCm has a typical $S = 1/2$ axial EPR signal with $g_{||} > g_{\perp} > 2.0$, indicating an x^2-y^2 ground state (vide infra).⁵⁰ (Throughout this study we use the abbreviated notation for d orbitals; e.g., x^2-y^2 for $d_{x^2-y^2}$.) The g values are large, and the metal hyperfine coupling constants are very small, with $|A_{||}| = 56 \times 10^{-4}$ cm $^{-1}$ and $|A_{\perp}|$ estimated to be less than 15×10^{-4} cm $^{-1}$. The spectra look similar to those of blue copper⁵¹ but with larger g values ($g_{||} = 2.350$ relative to

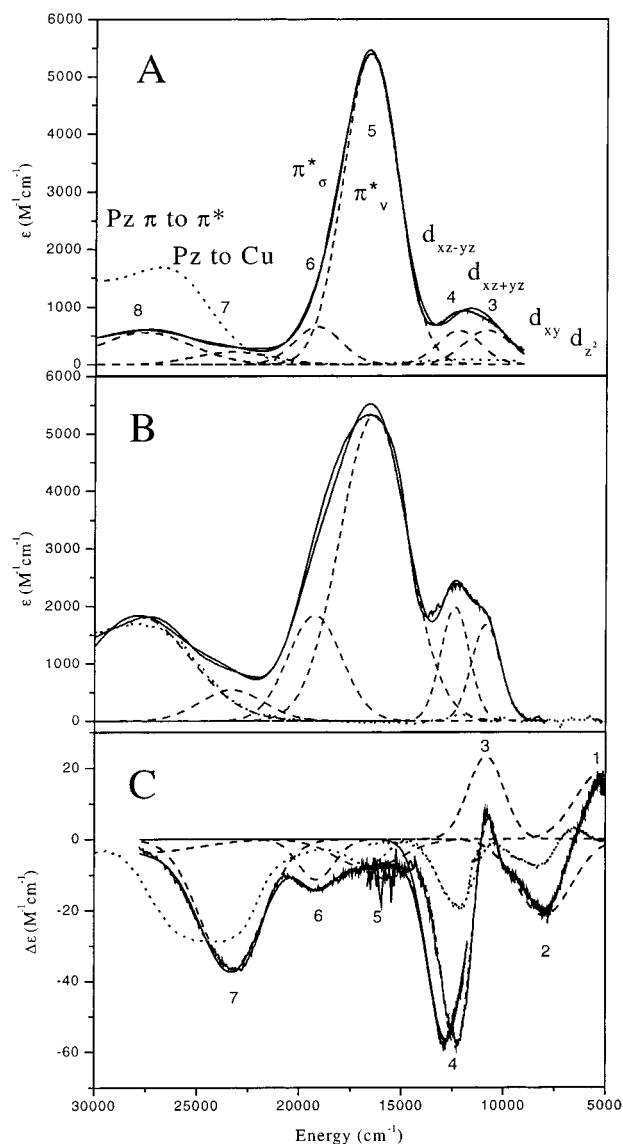


Figure 3. 220 K solution absorption in pentane (A), 120 K mull absorption (B), and 5 K, 7 T mull MCD (C) spectra of L3CuOOCm (solid lines) and L3CuOH (dotted lines). The Gaussian-resolved bands obtained from a simultaneous fit of the absorption and MCD spectra are shown by dashed lines along with their spectral assignments.

the blue copper site of plastocyanin with $g_{||} = 2.226$), suggesting a less covalent ground state (vide infra).⁵² The hydroperoxo Cu(II) complex, L3CuOOH, exhibits EPR features very similar to those of the alkylperoxo family (Figure 2B, Table 1), with large g values ($g_{||} = 2.380$, $g_{\perp} = 2.090$) and a small hyperfine splitting ($|A_{||}| \approx 40 \times 10^{-4}$ cm $^{-1}$).

Absorption and MCD. Both low-temperature (220 K) solution and low-temperature (120 K) mull absorption spectra were measured for each alkylperoxo complex. All alkylperoxo complexes look very similar. The spectra for L3CuOOCm are presented in Figure 3A,B along with the spectra of its synthetic starting material L3CuOH, in which the cumylperoxo ligand is replaced by a hydroxo group. The low-temperature mull absorption spectrum of L3CuOOCm is very similar to the solution spectrum, demonstrating that the molecular structure of this complex is maintained in solution. The solution absorption spectrum of L3CuOOCm is very different from that of its

(44) Neese, F.; Solomon, E. I. *J. Am. Chem. Soc.* **1998**, *120*, 12829.
 (45) Edwards, W. D.; Zerner, M. C. *Theor. Chim. Acta* **1987**, *72*, 347.
 (46) Heller, E. J. *Acc. Chem. Res.* **1981**, *14*, 368.
 (47) Tannor, D. T.; Heller, E. J. *J. Chem. Phys.* **1982**, *77*, 202.
 (48) Brunold, T. C.; Tamura, N.; Kitajima, N.; Moro-oka, Y.; Solomon, E. I. *J. Am. Chem. Soc.* **1998**, *120*, 5674.
 (49) For L1CuOOCm, the situation is complicated by the fact that the complex changes its coordination environment in solution at low temperature (<120 K), resulting in a different EPR signal. Therefore, the solid-state EPR data were used, and results similar to the first two complexes were obtained ($g_{||} = 2.316$, $g_{\perp} = 2.097$). The spectrum was not well resolved, and accurate metal hyperfine coupling constants could not be determined.
 (50) Solomon, E. I. *Comments Inorg. Chem.* **1984**, *3*, 227.
 (51) Solomon, E. I.; Hare, J. W.; Dooley, D. M.; Dawson, J. H.; Stephen, P. J.; Gray, H. B. *J. Am. Chem. Soc.* **1980**, *102*, 168.

(52) Solomon, E. I.; Hanson, M. A. In *Inorganic Electronic Structure and Spectroscopy*; Solomon, E. I., Lever, A. B. P., Eds.; John Wiley & Sons: New York, 1999; Vol. 2, pp 1–130.

Table 2. Summary of Gaussian-Resolved Absorption and MCD Bands of Alkylperoxo and Hydroperoxo Complexes^a

band	L3CuOOCm					L1CuOOCm				
	ν_{\max}	ϵ_{\max}	$\Delta\epsilon_{\max}$	10^3f	$\Delta\epsilon/\epsilon$	ν_{\max}	ϵ_{\max}	$\Delta\epsilon_{\max}$	10^3f	$\Delta\epsilon/\epsilon$
1, z^2	5 300		14.7			5 760		10.2		
2, xy	8 010		-17.3			8 050		-18.1		
3, $xz + yz$	10 855	590	18.6	7	0.032	11 140	220	10.3	3	0.047
4, $xz - yz$	12 225	585	-51.5	7	-0.088	12 670	470	-23.1	6	-0.049
5, π^*_v	16 590	5410	-6.6	79	-0.001	17 460	3815 ^b	-3.1	56	-0.001
6, π^*_σ	19 165	655	-9.1	8	-0.014	19 780	590	-1.2	9	-0.002

band	L3CuOOCtBu					L3CuOOH				
	ν_{\max}	ϵ_{\max}	$\Delta\epsilon_{\max}$	10^3f	$\Delta\epsilon/\epsilon$	ν_{\max}	ϵ_{\max}	$\Delta\epsilon_{\max}$	10^3f	$\Delta\epsilon/\epsilon$
1, z^2	5 000		5.9			5 000		1.6		
2, xy	7 870		-6.4			8 000		-1.5		
3, $xz + yz$	10 910	450	9.5	7	0.021	10 980	245	7.1	4	0.029
4, $xz - yz$	12 290	620	-30.8	8	-0.050	12 360	161	-9.5	2	-0.059
5, π^*_v	16 375	5000	-7.5	69	-0.002	16 560	1180 ^b	-2.7	19	-0.002
6, π^*_σ	18 615	855	-6.5	10	-0.008	17 970	435	-3.6	8	-0.008

^a Band maxima ν_{\max} in cm^{-1} , ϵ_{\max} and $\Delta\epsilon_{\max}$ in $\text{M}^{-1} \text{cm}^{-1}$, oscillator strength f , and $\Delta\epsilon/\epsilon$ ratio. ^b Underdetermined due to partial formation in solution.

hydroxo starting material L3CuOH. L3CuOOCm has an intense absorption band at $\sim 16\,600 \text{ cm}^{-1}$ (600 nm, $\epsilon = 5410 \text{ M}^{-1} \text{cm}^{-1}$), which gives rise to its dark blue color, and a weak band in the near-IR region at $\sim 12\,500 \text{ cm}^{-1}$ (800 nm, $\epsilon = \sim 580 \text{ M}^{-1} \text{cm}^{-1}$). In the UV region, a broad band is observed around $27\,000 \text{ cm}^{-1}$ for both L3CuOOCm and L3CuOH.

Figure 3C presents the mull MCD spectrum of L3CuOOCm at 5 K and 7 T, along with the MCD spectrum of L3CuOH.⁵³ Two positive and four negative bands are observed for L3CuOOCm. The first four bands (labeled 1–4) in the near-IR region are relatively intense and form two sets of pseudo-A term peaks. The two bands at $10\,850$ and $12\,225 \text{ cm}^{-1}$ (bands 3 and 4) correlate to the $\sim 12\,500 \text{ cm}^{-1}$ absorption band. This shows that this absorption feature is actually composed of two electronic transitions. The negative band at $\sim 19\,000 \text{ cm}^{-1}$ (band 6) is asymmetric and extends into the region of the broad intense $\sim 16\,600 \text{ cm}^{-1}$ absorption band. However, its minimum is shifted to higher energy by about 2500 cm^{-1} . This demonstrates that the intense $\sim 16\,600 \text{ cm}^{-1}$ absorption band also has two components. Resonance Raman profile data also support the presence of two transitions (vide infra). The highest energy negative feature (band 7) is very broad and fairly intense. The synthetic precursor L3CuOH also has an intense broad negative MCD band in this region.

Simultaneous fits of the absorption and MCD spectra of L3CuOOCm are obtained with a set of eight Gaussian-resolved bands (Figure 3). The transition energies, extinction coefficients, oscillator strengths, and $\Delta\epsilon/\epsilon$ ratios for the first six Gaussian-resolved bands of all these alkylperoxo complexes are given in Table 2.

Substitution of H for Cm yields very little changes in absorption and MCD spectra. Figure 4A shows the solution absorption spectrum of L3CuOOH at -50°C . Features similar to those of the alkylperoxo complexes are observed at energies below $22\,500 \text{ cm}^{-1}$: an intense absorption band at $16\,730 \text{ cm}^{-1}$ ($\sim 600 \text{ nm}$, $\epsilon = 1540 \text{ M}^{-1} \text{cm}^{-1}$) and a weaker band around $12\,000 \text{ cm}^{-1}$ ($\sim 830 \text{ nm}$, $\epsilon = \sim 300 \text{ M}^{-1} \text{cm}^{-1}$). The high-energy intense band at $\sim 27\,500 \text{ cm}^{-1}$ (360 nm) is due to the side-on (L3)Cu(μ - η^2 : η^2 -O₂)Cu(L3) dimer moiety which also forms in the solution, as it shows the characteristic resonance Raman features.^{7,54} Figure 4B shows the frozen glass MCD spectrum of L3CuOOH at 5 K and 7 T. Again, results very similar to those obtained for the alkylperoxo complexes were obtained.

(53) The mismatch of band 4 comes from an instrument artifact.

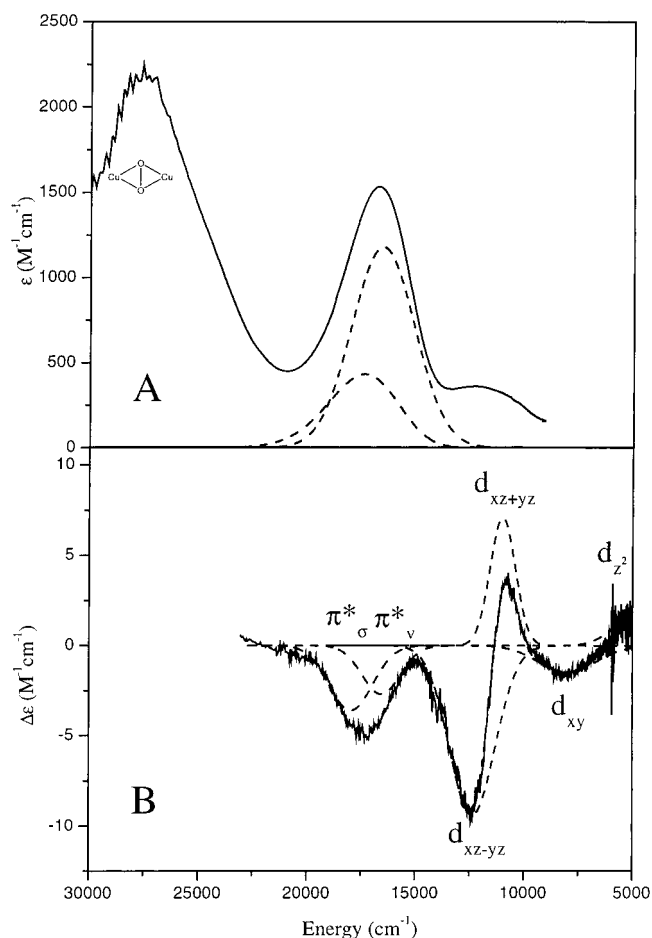


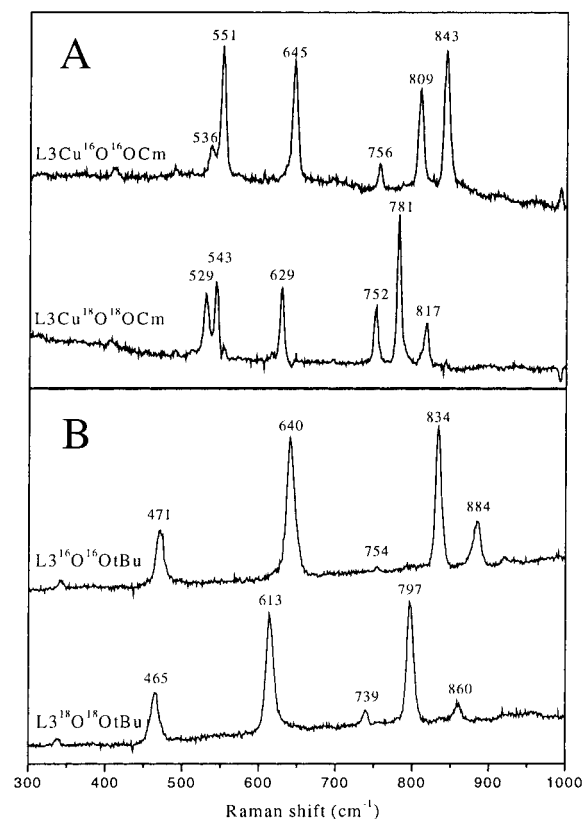
Figure 4. 220 K solution absorption spectrum in *tert*-butylbenzene (A), and 5 K, 7 T MCD spectrum in a toluene glass (B) of L3CuOOH. The Gaussian-resolved bands are shown in dashed lines along with their spectral assignments.

Relatively intense near-IR bands (two sets of pseudo-A term peaks) are observed at 5000 , 8000 , $10\,980$, and $12\,360 \text{ cm}^{-1}$.

(54) Three fundamental vibrational bands at 297 , 552 , and 736 cm^{-1} are observed at an excitation energy of 386 nm . The latter two shift to 525 and 697 cm^{-1} upon ^{18}O labeling. The 297 cm^{-1} vibration is strongly enhanced under the 360 nm absorption band. These three vibrational modes were previously assigned as Cu–Cu, symmetric Cu–O, and O–O vibration modes (see ref 7). The first overtone of the 552 cm^{-1} vibration is also observed at 1100 cm^{-1} and shifts to 1050 cm^{-1} in the ^{18}O -labeled sample.

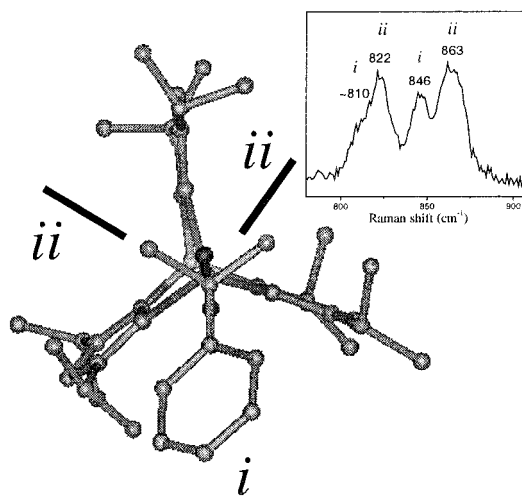
Table 3. Summary of Resonance Raman Vibrational Bands (cm^{-1})

L3CuOOCm			L1CuOOCm			L3CuOObu			L3CuOOH			
$^{16}\text{O}^{16}\text{O}$	$^{18}\text{O}^{18}\text{O}$	$\Delta\nu$	$^{16}\text{O}^{16}\text{O}$	$^{18}\text{O}^{18}\text{O}$	$\Delta\nu$	$^{16}\text{O}^{16}\text{O}$	$^{18}\text{O}^{18}\text{O}$	$\Delta\nu$	$^{16}\text{O}^{16}\text{O}$	$^{18}\text{O}^{18}\text{O}$	$\Delta\nu$	OOD
843	817	26	844	818	26	884	860	24	843	799	44	842
809	781	28	802	776	26	834	797	37				
756	752	4	755	749	6	754	739	15				
645	629	16	652	633	19	640	613	27	624	607	17	623
551	543	8	555	545	10	471	465	6				
536	529	7	540	536	4							

**Figure 5.** 77 K solid rR spectra of L3CuOOCm (A) and L3CuOObu (B) with excitation energy of 568.2 nm.

The latter two bands correlate with the weaker absorption band at $\sim 12\,000\text{ cm}^{-1}$. A negative MCD feature at $\sim 17\,500\text{ cm}^{-1}$ is also observed in the region of the intense $\sim 16\,730\text{ cm}^{-1}$ absorption band. In parallel to the alkylperoxy complexes, six bands are used to Gaussian-resolve the spectra, and their spectroscopic parameters are summarized in Table 2.

Resonance Raman. The resonance Raman spectrum of solid L3CuOOCm at 77 K obtained with an excitation at 568.2 nm ($17\,599\text{ cm}^{-1}$) is shown in the upper plot of Figure 5A. The spectrum is dominated by six bands at 843, 809, 756, 645, 551, and 536 cm^{-1} . In samples prepared with oxygen-18 (Figure 5A, lower plot), these bands shift to 817, 781, 752, 629, 543, and 529 cm^{-1} , respectively. There are also intensity changes upon oxygen-18 substitution. The three bands around the 800 cm^{-1} region show dramatic intensity redistribution, where the strongest band at 843 cm^{-1} decreases in intensity and the two lower energy vibrations increase in intensity. In addition, the intensity of the 645 cm^{-1} band decreases, and the two bands around the 540 cm^{-1} region change their relative intensities. In the region above 1000 cm^{-1} , weak vibrations are observed at 1108, 1156, and 1207 cm^{-1} . They show no shift upon oxygen-18 substitution and thus are not associated with the O–O moiety of the molecule (data not shown).

**Figure 6.** Side view of the crystal structure (position *i*) of L1CuOOCm and the possible conformational isomers (position *ii*) by rotating the C–O bond. Inset: 77 K L3CuOOCm rR spectrum in a CH_2Cl_2 glass excited at 568.2 nm.

L1CuOOCm has a solid rR spectrum very similar to that of L3CuOOCm (Figure S1 (Supporting Information), Table 3). Likewise, the L3CuOObu solid rR spectrum has features similar to those of the L3CuOOCm and L1CuOOCm spectra (Figure 5B, upper spectrum). However, the 800 cm^{-1} region of L3CuOObu has only two strong bands at 884 and 834 cm^{-1} , $\sim 35\text{ cm}^{-1}$ higher in energy than the corresponding bands of L3CuOOCm and L1CuOOCm. The relative band intensities are also different, with the 834 cm^{-1} band roughly 3 times more intense than the 884 cm^{-1} band. A weak but reproducible vibration at 754 cm^{-1} is also observed, which may correspond to the third band. In the lower energy region, only one band is present at 471 cm^{-1} instead of two bands at $\sim 540\text{ cm}^{-1}$, with about one-third of the intensity of the 640 cm^{-1} vibration. Upon ^{18}O substitution, all five bands shift to lower energy (860 , 797 , 739 , 613 , and 465 cm^{-1}), and vibrations in the 800 cm^{-1} region change in relative intensity. One weak combination band at 1112 cm^{-1} ($\approx 640 + 471\text{ cm}^{-1}$) is also observed which shifts to 1078 cm^{-1} ($\approx 613 + 465\text{ cm}^{-1}$) upon ^{18}O labeling (data not shown). Table 3 summarizes the rR vibrational results for all of the complexes.

The frozen glass rR spectrum of L3CuOOCm in CH_2Cl_2 was also obtained at an excitation energy of 568.2 nm ($17\,599\text{ cm}^{-1}$), and an interesting effect was observed in the 800 cm^{-1} region (Figure 6 inset, Figure S2). Each of the two strong vibrations which were observed in the solid rR spectrum is split into two bands at 810/822 and $846/863\text{ cm}^{-1}$, with an intensity ratio of roughly 1:2. Similar rR results were also obtained for L1CuOOCm in solution (Figure S3) but not for L3CuOObu (Figure S4). From the crystal structure of L1CuOOCm (Figure 1), the split peaks appear to be associated with conformational isomers of the cumylperoxide ligand in solution. There are three

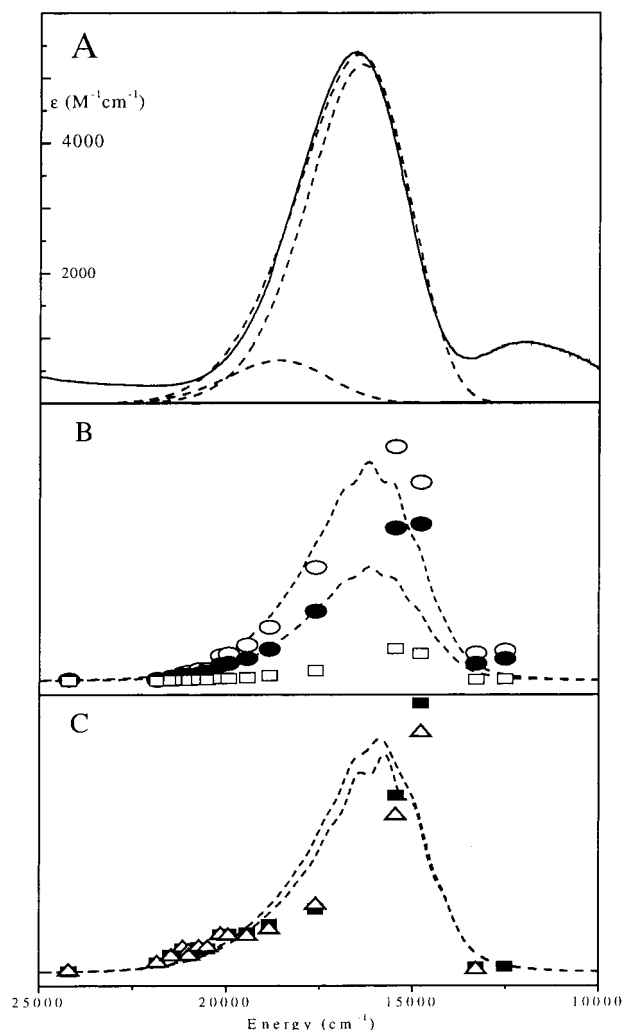


Figure 7. (A) 220 K solution absorption spectrum of L3CuOOCm (solid line) and simulated spectrum (dashed line), obtained from the sum of two CT bands calculated with the fitted parameters in Table 8. (B) 77 K experimental rR excitation profiles for the 843 (○), 809 (●), and 756 (□) cm^{-1} vibrations of solid L3CuOOCm and simulated profiles of 843 and 809 cm^{-1} vibrations for the two CT transitions (dashed lines). (C) As in B, for 644 (■) and 551 (△) cm^{-1} vibrations.

local energy minima associated with rotation of the O—C bond: one observed in the crystal structure and two others between neighboring pyrazole rings which are indicated by solid bars in Figure 6. The latter two (orientation *ii* in Figure 6) are almost identical but symmetrically inequivalent to the orientation *i*. These two equivalent conformational isomers will give an additional set of vibrational bands twice as intense as the original vibrations and higher in energy due to steric constraints. In contrast, the three methyl groups in L3CuOOtBu are identical, and only one set of rR vibrational bands was observed for this complex in solution.

In Figure 7, the resonance Raman excitation profiles for 843, 809, 756, 645, and 551 cm^{-1} vibrations of solid L3CuOOCm at 77 K are plotted with the corresponding absorption spectrum. The profiles are grouped into two plots for clarity. The excitation profile for the 536 cm^{-1} vibration could not be obtained due to its low intensity and significant overlap with the 551 cm^{-1} vibration. All vibrations are resonance enhanced under the intense absorption band at $\sim 16\,600\text{ cm}^{-1}$, with stronger enhancement on the low-energy side.⁵⁵ The profiles for the 644 and 551 cm^{-1} vibrations show a clear shoulder on the high-energy side, demonstrating that there are at least two electronic

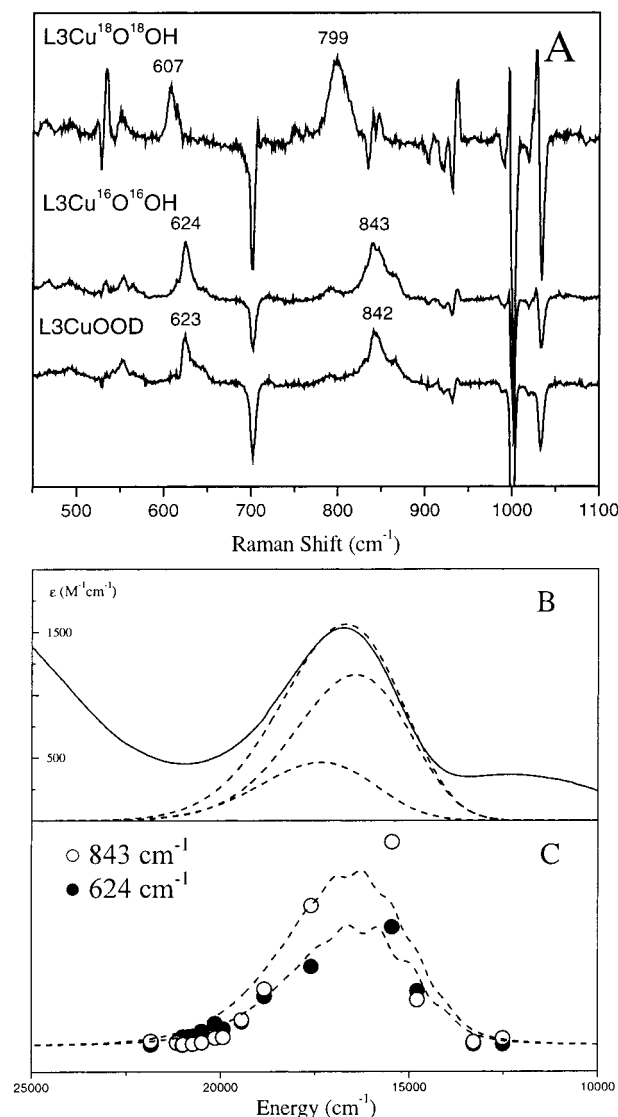


Figure 8. (A) 77 K rR spectra of L3Cu¹⁸O¹⁸OH (upper), L3CuOOH (middle), and L3CuOOD (lower) excited at 568.2 nm in a *tert*-butylbenzene glass. (B) 220 K solution absorption spectrum (solid line) of L3CuOOH in *tert*-butylbenzene and simulated spectrum (dashed lines) from the sum of two CT bands with the fitted parameters in Table 8. (C) 77 K rR excitation profiles of 624 (●) and 843 (○) cm^{-1} vibrations of L3CuOOH in a *tert*-butylbenzene glass and simulated profiles (dashed lines).

transitions under the absorption band at $\sim 16\,600\text{ cm}^{-1}$. This is consistent with the results obtained from a simultaneous Gaussian fit of the absorption and MCD spectra (Figure 3).

The rR excitation profiles for the corresponding vibrations of L1CuOOCm (Figure S5) and L3CuOOtBu (Figure S6) closely resemble those of L3CuOOCm.

The rR spectrum of L3CuOOH in a *tert*-butylbenzene glass at 77 K obtained with an excitation at 568.2 nm ($17\,599\text{ cm}^{-1}$) is much simpler than those of the alkylperoxo complexes and is dominated by two vibrations at 624 and 843 cm^{-1} (Figure 8A, middle spectrum, and Table 3). (Note: the sharp derivative and negative features are artifacts due to subtraction of the *tert*-butylbenzene solvent bands.) Upon oxygen-18 substitution, these features shift to 607 and 799 cm^{-1} (Figure 8A, upper spectrum,

(55) Note that the red shift of the profile relative to the absorption band is due to the fact that the Raman intensities were quantitated relative to an internal standard, which eliminates their ν^4 dependence, whereas the absorption intensity scales linearly with ν .

and Table 3). In samples prepared with D₂O₂, bands are observed at 623 and 842 cm⁻¹ (Figure 8A, lower spectrum, and Table 3). Excitation profiles of the 624 and 843 cm⁻¹ vibrations of L3CuOOH are plotted with the corresponding absorption spectrum in Figure 8B,C. Both vibrational features are resonance enhanced, with profiles following the absorption band shape.

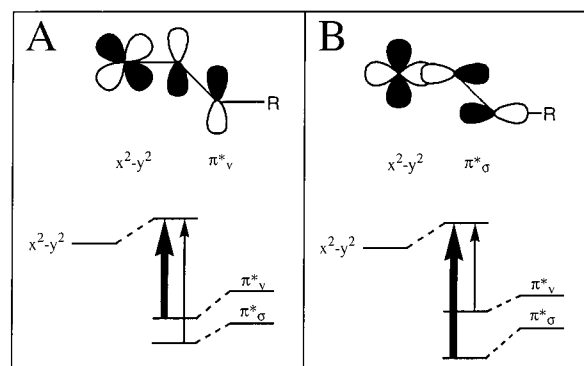
Analysis

1. Spectroscopic Assignments. Table 2 summarizes the Gaussian-resolved transitions, oscillator strengths, f , and $\Delta\epsilon/\epsilon$ (i.e., MCD-to-absorption intensity) ratios obtained from the absorption and MCD spectra of L3CuOOCm (Figure 3). At 5 K and 7 T, the MCD spectrum is dominated by C terms. These require two perpendicular transition moments. Yet in C_1 symmetry, all transitions are nondegenerate and have unidirectional transition moments. Thus, the C term MCD intensity derives from the spin-orbit coupling between the nondegenerate excited states. The magnitude of the $\Delta\epsilon/\epsilon$ ratio for each transition strongly depends on the magnitude of spin-orbit coupling. States mainly centered on atoms with higher spin-orbit coupling constants will have larger $\Delta\epsilon/\epsilon$ ratios than those centered on atoms with small spin-orbit coupling constants.⁵⁶ The first four transitions (bands 1–4) are intense in the low-temperature MCD spectrum relative to the absorption spectrum and thus are assigned as the ligand field (d–d) transitions of the copper center ($\xi_{\text{Cu}} \approx 830$ cm⁻¹, $\xi_{\text{O,N}} \approx 100$ cm⁻¹). Previously, ligand field and molecular orbital calculations combined with group-theory-derived selection rules have been used to assign the ligand field transitions of the rhombically perturbed C_{3v} elongated T_d site of blue copper proteins on the basis of their MCD signs and C/D ratios.⁵⁶ The mononuclear alkylperoxo Cu(II) complex system studied here has the same effective symmetry (Figure 1) and shows a ligand field pattern (signs and intensities) very similar to that of the well-characterized blue copper centers^{51,56,57} (Figure 3 and Table 2). Therefore, bands 1–4 are similarly assigned as the Cu z^2 (+), xy (–), $xz+yz$ (+), and $xz-yz$ (–) $\rightarrow x^2-y^2$ transitions, respectively (Figure 3).

Band 7, which is intense in MCD and also appears in the hydroxide analogue L3CuOH, is assigned as a pyrazolyl ligand-to-Cu(II) CT transition. Band 8 has a fair amount of absorption intensity but no MCD intensity and thus is assigned as a pyrazole ligand π -to- π^* transition.

Bands 5 and 6 have very small $\Delta\epsilon/\epsilon$ ratios and are absent in the absorption spectrum of the hydroxide precursor (Figure 3A,B). Thus, they are assigned as alkylperoxide-to-Cu(II) CT transitions. The highest occupied orbitals of free peroxide are the doubly degenerate π^* set. The two π^* orbitals split in energy due to σ -bonding to the carbon sp^3 hybrid orbital of the alkyl group. The bonding π^* orbital (referred to as π^*_σ) is stabilized in energy, while the other π^* orbital (referred to as π^*_v) is nonbonding and thus at higher energy. In the crystal structure of L1CuOOCm, the Cu–O–O angle is 112.1°, and the dihedral angle of Cu–O–O–C is close to 180°. The π^*_σ orbital is oriented in the approximate Cu–O–O–C plane and can contribute a σ -bonding interaction to the Cu(II) center. The π^*_v orbital is located perpendicular to the Cu–O–O–C plane and can have a π -bonding interaction with Cu(II). From the EPR results ($g_{\parallel} > g_{\perp} > 2.0$),^{50,52} the half-occupied orbital on the Cu is x^2-y^2 , and the relative intensities of the π^*_v/π^*_σ CT transitions should reflect their relative overlaps with the Cu x^2-y^2 orbital and hence the orientation of Cu x^2-y^2 orbital relative to the

Scheme 1



Cu–O bond. If the lobe of the x^2-y^2 orbital is along the Cu–OOR bond, the higher energy π^*_σ CT transition should be more intense (Scheme 1B). Alternatively, if the lobes of the x^2-y^2 orbital are bisected by the Cu–OOR bond, the lower energy π^*_v CT transition should be more intense (Scheme 1A). From Figure 3 and Table 2, the latter case is observed for L3CuOOCm. One strong CT absorption band occurs at 16 590 cm⁻¹, and a second weak CT band is observed at 19 165 cm⁻¹. This demonstrates that the dominant interaction between the alkylperoxide π^* and the Cu x^2-y^2 orbitals is the π -bond. Therefore, bands 5 and 6 are assigned as CT transitions from π^*_v and π^*_σ orbitals of the alkylperoxide to the Cu x^2-y^2 orbital, respectively. (Note the molecular coordinate system is defined so that the Cu–O bond bisects the x and y axes, and the z axis is perpendicular to the approximate equatorial plane formed by the Cu–O and two short Cu–N bonds. This is shown in Figure 1.) These assignments are further supported by the resonance Raman results (Figure 7, vide infra).

The electronic transitions of L3CuOOH below 22 500 cm⁻¹ (Figure 4) are assigned in a similar way.

2. EPR Parameters. The g values of L3CuOOCm ($g_{\parallel} = 2.350$ and $g_{\perp} = 2.076$) are large compared to those of normal tetragonal Cu(II) complexes (e.g., for D_{4h} CuCl_4^{2-} molecule, $g_{\parallel} = 2.221$ and $g_{\perp} = 2.040$ ⁵⁰). The ligand field expressions for the g values associated with the unpaired electron in the x^2-y^2 orbital are

$$g_{\parallel} = 2.0023 - \frac{8\lambda\alpha_1^2\beta_1^2}{E_{xy} - E_{x^2-y^2}} \quad (2a)$$

$$g_{\perp} = 2.0023 - \frac{2\lambda\gamma_1^2\beta_1^2}{E_{xz,yz} - E_{x^2-y^2}} \quad (2b)$$

where $\lambda(\text{Cu}^{\text{II}}) \approx -830$ cm⁻¹, β_1 , α_1 , and γ_1 are the metal x^2-y^2 , xy , and xz/yz orbital coefficients in the ligand field wave functions. $E_{x^2-y^2}$, E_{xy} , and $E_{xz,yz}$ ($= (E_{xz} + E_{yz})/2$) are the ligand field state energies. (Note: axial effective symmetry is used here since the splitting of g_x and g_y is not experimentally resolved.) Taking $\alpha_1^2/\beta_1^2 = 1.082$ (from INDO/S-CI calculations, Table S3, vide infra), the experimental g values give an estimate of the ground-state (x^2-y^2) Cu character, $\beta_1^2 \approx 0.62$.⁵⁸ This calculated covalency is similar to that of D_{4h} CuCl_4^{2-} , which has 63% Cu character in the ground state.⁵⁰ However, for the alkylperoxo complexes, this covalency is localized along the Cu–OOR bond, while in D_{4h} CuCl_4^{2-} it is delocalized equivalently over four chloride ligands. The large g values of alkylperoxo complexes thus do not reflect a reduced covalent interaction (i.e., larger β^2) with the ligands but arise from the

(56) Gewirth, A. A.; Solomon, E. I. *J. Am. Chem. Soc.* **1988**, *110*, 3811.

(57) Penfield, K. W.; Gewirth, A. A.; Solomon, E. I. *J. Am. Chem. Soc.* **1985**, *107*, 4519.

low energy of the ligand field (d–d) transitions due to the distorted tetrahedral symmetry. (The Cu d–d transitions in D_{4h} CuCl_4^{2-} are at 12 500 (xy), 14 250 (xz , yz), and 17 000 (z^2) cm^{-1} ,⁵⁹ while for L3CuOOCm they are at 5300 (z^2), 8010 (xy), 10 855 ($xz+yz$), and 12 225 ($xz-yz$) cm^{-1} .) This results in larger excited-state spin–orbit coupling into the ground state, which leads to the larger g values.

The hyperfine coupling of alkylperoxo complexes is significantly smaller than that of D_{4h} CuCl_4^{2-} (for L3CuOOCm , $|A_{||}| = 56 \times 10^{-4} \text{ cm}^{-1}$ and $|A_{\perp}| < 15 \times 10^{-4} \text{ cm}^{-1}$; for D_{4h} CuCl_4^{2-} , $A_{||} = -164 \times 10^{-4} \text{ cm}^{-1}$ and $A_{\perp} = -35 \times 10^{-4} \text{ cm}^{-1}$). In blue copper sites, the small hyperfine coupling is associated with a highly covalent ground state of $\sim 40\%$ Cu character,⁵² which is not the case for the alkylperoxo Cu(II) complexes studied here. From ligand field theory, the metal hyperfine coupling is given by

$$A_{||} = Pd \left[-\kappa\beta^2 - \frac{4}{7}\beta^2 + (g_{||} - 2.0023) + \frac{3}{7}(g_{\perp} - 2.0023) \right] \quad (3a)$$

$$A_{\perp} = Pd \left[-\kappa\beta^2 + \frac{2}{7}\beta^2 + \frac{11}{14}(g_{\perp} - 2.0023) \right] \quad (3b)$$

where $Pd[\text{Cu(II)}] \approx 400 \times 10^{-4} \text{ cm}^{-1}$ and $\kappa[\text{Cu(II)}] \approx 0.43$. From these equations, the terms containing the g values (i.e., indirect dipolar coupling term due to orbital angular momentum spin–orbit mixed into the ground state) oppose the contributions from the Fermi contact and spin dipolar terms. Therefore, the large g values for alkylperoxo Cu(II) complexes will result in a smaller value of $A_{||}$ without an increase in covalency relative to D_{4h} CuCl_4^{2-} . Using eq 3, $A_{||}$ and A_{\perp} are estimated to be -96×10^{-4} and $-13 \times 10^{-4} \text{ cm}^{-1}$, respectively. These values are significantly reduced from those of D_{4h} CuCl_4^{2-} , although not to the experimental values.⁶⁰ Thus, the small metal hyperfine coupling is due not to high covalency but rather to the large g values that result from the low energies of the d–d excited states in the distorted tetrahedral ligand field.

Similar analysis gives $\sim 65\%$ Cu character in the ground state of L3CuOOH .

3. Resonance Raman. 3.1. Vibrational Assignments and Normal Coordinate Analyses. For L3CuOOCm , six bands in the resonance Raman spectrum (Figure 5A, Table 3) show isotope shifts upon ^{18}O substitution and resonance enhancement under the alkylperoxide π^* -to-Cu x^2-y^2 CT bands. Thus, they are all related to the Cu–O–O unit in the molecule. Three bands (843, 809, and 756 cm^{-1}) are observed in the 800 cm^{-1} region, where the vibrations of O–O, C–O, and C–C stretching are all expected to contribute and can be highly coupled. On the basis of the rR excitation profiles, isotope shifts ($\Delta\nu(^{16}\text{O}_2/^{18}\text{O}_2) = 26, 28$, and 4 cm^{-1} , respectively), and similar vibrational analyses on related Fe(III) alkylperoxo complexes,^{61–64} these three bands are assigned as mixed O–O/C–O/C–C vibrations in which the O–O percentage determines the isotope shifts

and rR intensities (i.e., the 756 cm^{-1} vibration contains the least O–O character.) Similar assignments apply to the three vibrations around 800 cm^{-1} for L1CuOOCm and L3CuOObu . The 645 cm^{-1} (652 cm^{-1} in L1CuOOCm , 640 cm^{-1} in L3CuOObu) vibration is assigned as the dominantly Cu–O stretching mode on the basis of its frequency and isotope shift ($\Delta\nu = 16 \text{ cm}^{-1}$).

The lower energy vibrations are more difficult to assign. Que and co-workers have synthesized a *tert*-butylperoxo high-spin Fe(III) complex $[\text{Fe}(\text{6-Me}_3\text{TPA})(\text{H}_2\text{O})(\text{OObu})](\text{ClO}_4)_2$,^{62–64} which shows rR features similar to those of L3CuOObu . Four bands are observed in the rR spectrum at 876, 842, 637, and 469 cm^{-1} with the same intensity pattern as that of L3CuOObu . The 469 cm^{-1} vibration shifts to 422 cm^{-1} in the sample prepared with $\text{tBuOOH-}d_9$ ($\Delta\nu = 47 \text{ cm}^{-1}$). On the basis of this isotope shift and the low frequency (below 500 cm^{-1}), this vibration was assigned mainly as the C–C–C deformation of the *tert*-butyl group. By analogy, the 471 cm^{-1} vibration in L3CuOObu is similarly assigned here. The 551 and 536 cm^{-1} vibrations in L3CuOOCm are also assigned as mainly carbon skeleton deformation modes, and the increased frequencies relative to that of L3CuOObu are ascribed to the contribution from the benzene ring vibrations. The resonance Raman intensity of the 551 cm^{-1} vibration is attributed to a mixing of the Cu–O stretch distortion into this mode, since the excitation profile of the 551 cm^{-1} vibration parallels that of the 645 cm^{-1} vibration, and thus the intensities in both modes reflect a distortion along the Cu–O bond. Compared to L3CuOOCm , the 471 cm^{-1} vibration of L3CuOObu is 75 cm^{-1} further separated from the main Cu–O vibration at 640 cm^{-1} , and thus they are less coupled, resulting in the reduced intensity of the 471 cm^{-1} vibration relative to that of the 551 cm^{-1} vibration in L3CuOOCm .

The rR spectrum of the hydroperoxo complex L3CuOOH is much simpler (Figure 8A). Two bands are observed at 843 and 624 cm^{-1} and are assigned as O–O and Cu–O stretching vibrations on the basis of their frequencies and isotope shifts ($\Delta\nu(^{16}\text{O}_2/^{18}\text{O}_2) = 44$ and 17 cm^{-1}). The $\nu(^{16}\text{O}_2)/\nu(^{18}\text{O}_2)$ ratio is 1.055, very close to the harmonic value ($=1.061$) with oxygen motion only, indicating an isolated O–O stretching vibration. The shifts upon deuteration of the hydroperoxo ligand are very small ($\Delta\nu = 1 \text{ cm}^{-1}$) but are consistent with previous rR studies on the Fe(III)–OOH complex,^{65,66} where the deuterium isotope shifts for O–O and Fe–O vibrations are 0 and 5 cm^{-1} , respectively. It is important to note that in the μ -1,1-bridged complex Cu_2OOH , the O–O vibration was at 880 cm^{-1} , 37 cm^{-1} higher than that of L3CuOOH (vide infra).³⁰

A normal coordinate analysis was performed on the simplified N_3CuOOC_3 unit in L3CuOOCm using the Raman data presented in Table 3 and the crystal structure of L1CuOOCm . The pyrazolyl ring mass (68 amu) was used for the terminal nitrogens, and the methyl group mass (15 amu) and benzene

(58) Note that the covalency estimate from eq 2 is, in fact, an upper limit (i.e., a lower limit of β^2). This is because eq 2 does not include ligand orbital momentum and related contributions to β^2 . In the cases where this has been evaluated for Cu complexes, it is calculated to be small (1–5%) and increase β^2 . See, for example: (a) Penfield, K. W.; Gewirth, A. A.; Solomon, E. I. *J. Am. Chem. Soc.* **1985**, *107*, 4519. (b) Gewirth, A. A.; Cohen, S. L.; Schugar, H. J.; Solomon, E. I. *Inorg. Chem.* **1987**, *26*, 1133. (c) Lupe, A.; McMillan, J. A. *J. Chem. Phys.* **1972**, *57*, 827. (d) Smith, D. W. *J. Chem. Soc. A* **1970**, 3108.

(59) Hitchman, M. A.; Cassidy, P. J. *Inorg. Chem.* **1979**, *18*, 1745.

(60) Note that in eq 3 the experimental g values should be corrected for ligand contributions. This reduces the calculated $|A_{||}|$ value by $\sim 20 \times 10^{-4} \text{ cm}^{-1}$. See ref 58b.

(61) Lehnert, N.; Ho, R. Y. N.; Que, L., Jr.; Solomon, E. I., manuscript in preparation.

(62) Zang, Y.; Elgren, T. E.; Dong, Y.; Que, L., Jr. *J. Am. Chem. Soc.* **1993**, *115*, 811.

(63) Zang, Y.; Kim, J.; Dong, Y.; Wilkinson, E. C.; Appelman, E. H.; Que, L., Jr. *J. Am. Chem. Soc.* **1997**, *119*, 4197.

(64) Kim, J.; Larka, E.; Wilkinson, E. C.; Que, L., Jr. *Angew. Chem., Int. Ed. Engl.* **1995**, *34*, 2048.

(65) Ho, R. Y. N.; Roelfes, G.; Feringa, B. L.; Que, L., Jr. *J. Am. Chem. Soc.* **1999**, *121*, 264.

(66) Roelfes, G.; Lubben, M.; Chen, K.; Ho, R. Y. N.; Meetsma, A.; Genseberger, S.; Hermant, R. M.; Hage, R.; Mandal, S. K.; Young, V. G., Jr.; Zang, Y.; Kooijman, H.; Spek, A. L.; Que, L., Jr.; Feringa, B. L. *Inorg. Chem.* **1999**, *38*, 1929.

Table 4. Observed and Calculated Vibrational Frequencies (cm^{-1}), Potential Energy Distribution (%) and Selected Force Constants (Stretching, $\text{mdyn}/\text{\AA}$; Bending, $\text{mdyn}/\text{\AA}$) of L3CuOOcM NCA

normal mode ^a	frequencies		potential energy distribution							
	exptl	NCA	$\Delta r_{\text{Cu-O}}$	$\Delta r_{\text{O-O}}$	$\Delta r_{\text{O-C}}$	$\Delta r_{\text{C-C}}$	$\Delta \theta_{\text{Cu-O-O}}$	$\Delta \theta_{\text{O-O-C}}$	$\Delta \theta_{\text{C-C-C}}$	$\Delta \theta_{\text{O-C-C}}$
$\text{L3Cu}^{16}\text{O}^{16}\text{OCm}$										
$\nu(\text{O-O})$	843	844	7	46	21	10	0	1	6	6
$\nu(\text{O-C})$	809	809	9	20	50	9	1	4	2	3
$\nu(\text{C-C})$	756	758	1	10	18	33	0	9	9	18
$\nu(\text{Cu-O})$	645	649	57	7	2	16	2	5	8	1
$\delta(\text{C-C-C})$	551	552	1	0	16	9	2	4	54	12
$\delta(\text{O-C-C})$	536	538	0	0	0	8	0	0	15	72
$\text{L3Cu}^{18}\text{O}^{18}\text{OCm}$										
$\nu(\text{O-C})$	817	818	2	16	45	12	0	1	10	12
$\nu(\text{O-O})$	781	776	16	37	25	14	1	5	1	0
$\nu(\text{C-C})$	752	746	0	21	16	30	0	7	8	16
$\nu(\text{Cu-O})$	629	624	57	8	2	13	2	7	7	0
$\delta(\text{C-C-C})$	543	542	2	0	20	7	2	4	53	11
$\delta(\text{O-C-C})$	529	529	0	0	0	8	0	0	18	71
force constants			3.03	3.22	3.60		0.294	1.41		

^a Normal modes are labeled according to their dominant characters of PED.**Table 5.** Selected L3CuOOcM NCA Mass-Weighted Eigenvectors \mathbf{L}_n Containing the Cu-O-O-C Unit

normal mode	eigenvectors				
	$\Delta r_{\text{Cu-O}}$	$\Delta r_{\text{O-O}}$	$\Delta r_{\text{O-C}}$	$\Delta \theta_{\text{Cu-O-O}}$	$\Delta \theta_{\text{O-O-C}}$
$\nu(\text{O-O})$	-0.105	0.260	0.167	-0.079	-0.055
$\nu(\text{O-C})$	-0.120	0.171	-0.252	0.122	0.110
$\nu(\text{Cu-O})$	0.217	0.073	-0.038	-0.122	-0.096
$\delta(\text{C-C-C})$	0.025	-0.008	-0.083	0.098	0.069

ring mass (77 amu) were used for the terminal carbons in the simplified NCA model. A generalized valence force field (GVFF) was used, allowing for the inclusion of some results from a quantum-chemistry-calculated force field. Although the $\text{N}_3\text{CuOOCC}_3$ is a simplified model, it is still a large system with 24 vibrational degrees of freedom, and the large number of force constants needed to construct a complete force field is underdetermined by the data. These force constants were estimated from quantum mechanical frequency calculations.⁶⁷

The fitted vibrational frequencies and potential energy distributions are summarized in Table 4. Table 5 gives the mass-weighted eigenvectors for selected normal modes. The complete force field is summarized in Table S1. The calculated frequencies and isotope shifts reproduce the experimental values very well. The fitted O–O force constant is 3.22 $\text{mdyn}/\text{\AA}$, close to the high end of known O–O force constants for copper peroxide complexes^{7,30,68,69} showing a strong O–O bond. The fitted Cu–O force constant is 3.03 $\text{mdyn}/\text{\AA}$, also indicating a strong bond. For the three vibrations in the 800 cm^{-1} region, the NCA reproduces not only the frequencies very well, but also the intensity distributions. The rR intensity is proportional to the Cu–O and O–O contributions in the normal mode. The 843 cm^{-1} vibration has the most Cu–O and O–O character (7% Cu–O + 46% O–O) and is thus the most intense. The 756 cm^{-1} vibration only has 1% Cu–O and 10% O–O character and is thus the least intense in the rR spectrum. Upon oxygen-18 substitution, the O–O potential energy distribution dramatically changes over these three vibrations. The middle vibration gains significant O–O character and has the highest resonance

intensity in this region. The 817 cm^{-1} vibration loses most of its O–O character and becomes the weakest peak. The 752 cm^{-1} vibration gains O–O character and becomes more intense than the 817 cm^{-1} peak.

The NCA assigns the two lower energy vibrations (551 and 536 cm^{-1}) as mainly C–C–C and O–C–C deformation modes and predicts the observed isotope shifts, but the resonance intensities of these peaks are not consistent with the experimental results. The excitation profiles indicate that the resonance enhancements of these two vibrations are similar to that of the 645 cm^{-1} vibration (Cu–O stretch), and the intensity increase upon ^{18}O labeling should reflect increased mixing with the Cu–O stretch due to its reduced vibrational frequency. While the NCA reproduces the trend, the calculated contribution is too small. This problem is due to our simplified NCA model, which does not allow for an accurate description of the ring contributions, while in reality the change from a cumyl to a *tert*-butyl group shows an effect on the rR spectra in Figure 5.

Quantum chemistry frequency-calculation-assisted NCA was also applied to L3CuOOH , and the resulting fits obtained using the NCA model N_3CuOOH are summarized in Tables 6 and 7. The complete force field is given in Table S2. The calculated force constants for O–O and Cu–O are 3.51 and 2.94 $\text{mdyn}/\text{\AA}$, also indicating strong O–O and Cu–O bonds. The potential energy distributions in Table 7 show that both the Cu–O and O–O vibrations are much more localized in the hydroperoxo than in the alkylperoxo complexes, consistent with the simpler resonance Raman spectra for the hydroperoxo complex in Figure 8.

Surprisingly, although there is a large frequency difference (37 cm^{-1}) between the O–O vibrations of L3CuOOH and $\text{Cu}_2\text{-OOH}$, the force constants of the O–O stretch are almost the same for these two hydroperoxo complexes (Table 9). From the crystal structures of the corresponding alkylperoxo and acylperoxo complexes (L1CuOOcM and Cu_2OOR , where $\text{R} = m\text{-ClC}_6\text{H}_4\text{C(O)-}$), the Cu–O–O angle of Cu_2OOR is $\sim 11^\circ$ larger than that of L1CuOOcM .^{26,28} Previous studies have shown that the mechanical coupling between the metal–O and O–O vibrations strongly depends on the metal–O–O angle; a larger metal–O–O angle results in a higher O–O vibrational frequency for the same O–O force constant.⁴⁸ Thus, the higher frequency of the O–O vibration of Cu_2OOH relative to that of L3CuOOH does not reflect a stronger bond but is due to the

(67) Lehnert, N.; Tuzcek, F. *Inorg. Chem.* **1999**, 38, 1659.(68) Baldwin, M. J.; Ross, P. K.; Pate, J. E.; Tyeklár, Z.; Karlin, K. D.; Solomon, E. I. *J. Am. Chem. Soc.* **1991**, 113, 8671.(69) Pate, J. E.; Cruse, R. W.; Karlin, K. D.; Solomon, E. I. *J. Am. Chem. Soc.* **1987**, 109, 2624.

Table 6. Observed and Calculated Vibrational Frequencies (cm⁻¹) and Selected Force Constants (Stretching, mdyn/Å; Bending, mdyn·Å) of L3CuOOH NCA

normal mode	L3Cu ¹⁶ O ¹⁶ OH		L3Cu ¹⁸ O ¹⁸ OH		L3CuOOD		NCA force constants
	exptl	NCA	exptl	NCA	exptl	NCA	
$\nu(\text{O}-\text{H})$		3602		3589		2622	$k_{\text{O}-\text{H}} = 7.19$
$\delta(\text{O}-\text{O}-\text{H})$		1290		1284		955	$k_{\text{O}-\text{O}-\text{H}} = 0.88$
$\nu(\text{O}-\text{O})$	843	845	799	798	842	841	$k_{\text{O}-\text{O}} = 3.51$
$\nu(\text{Cu}-\text{O})$	624	627	607	605	623	621	$k_{\text{Cu}-\text{O}} = 2.94$
$\delta(\text{Cu}-\text{O}-\text{O})$		177		172		176	$K_{\text{Cu}-\text{O}-\text{O}} = 0.27$

Table 7. L3CuOOH NCA Potential Energy Distributions (%) and Mass-Weighted Eigenvectors (\mathbf{L}_n)

normal mode	internal coordinate				
	$\Delta r_{\text{Cu}-\text{O}}$	$\Delta r_{\text{O}-\text{O}}$	$\Delta r_{\text{O}-\text{H}}$	$\Delta \theta_{\text{Cu}-\text{O}-\text{O}}$	$\Delta \theta_{\text{O}-\text{O}-\text{H}}$
Potential Energy Distribution (%)					
$\nu(\text{O}-\text{O})$	10	82	0	0	7
$\nu(\text{Cu}-\text{O})$	77	11	0	4	2
Eigenvectors					
$\nu(\text{O}-\text{O})$	-0.131	0.343	0.004	-0.057	-0.200
$\nu(\text{Cu}-\text{O})$	0.236	0.081	-0.008	-0.172	-0.067

increased mechanical coupling between the Cu–O and O–O vibrations.

3.2. Excited-State Distortions from rR Profiles. The electronic absorption band shape and rR excitation profiles were analyzed within the framework of time-dependent Heller theory, which provides the molecular distortions in the excited states.^{46,47,70,71} In this formalism, the absorption spectrum for an electronic transition to an excited state r is given by

$$I(\nu) \propto \nu \int_{-\infty}^{\infty} \langle \phi | \phi(t) \rangle_r \exp[i\nu t] dt \quad (4)$$

where $I(\nu)$ is the absorption intensity at energy ν . The wave packet overlap $\langle \phi | \phi(t) \rangle_r$ has the form

$$\langle \phi | \phi(t) \rangle_r = \exp \left[\sum_n \left(-\frac{\Delta_{n,r}^2}{2} (1 - \exp(-i\nu_n t)) - \frac{i\nu_n t}{2} \right) - iE_{0,r}t - \Gamma_r^2 t^2 \right] \quad (5)$$

where ν_n is the vibrational frequency of the n th normal mode and $\Delta_{n,r}$ is the dimensionless displacement of state r relative to the ground state along mode n . The parameter $E_{0,r}$ is the energy of the zero-phonon transition to state r , and Γ_r is a damping factor that governs the resolution of vibrational structure. A spectrum with several overlapping absorption bands is given by the sum of individual spectra calculated with eq 4.

The general expression for Raman polarizability α for k electronic excited states is given by the half-Fourier transform,

$$\alpha_{i \rightarrow f}(\nu_i) = \frac{i}{\hbar} \int_0^{\infty} \left(\sum_{r=1}^k \mu_r^2 \langle \phi_f | \phi(t) \rangle_r \exp[-iE_{0,r}t - \Gamma_r t] \right) \exp[i\nu_i t] dt \quad (6)$$

where μ_r is the transition dipole moment for the electronic transition from the ground state to the excited state r ($\mu_r^2 \propto f_r$)

(70) Myers, A. B.; Mathies, R. A. In *Biological Application of Raman Spectroscopy*; Spiro, T. G., Ed.; Wiley: New York, 1987; Vol. 2, pp 1–58.

(71) Shin, K.-S. K.; Zink, J. I. *Inorg. Chem.* **1989**, 28, 4358.

and ν_i is the energy of the incident laser radiation. The time-dependent overlap is given by

$$\langle \phi_f | \phi(t) \rangle_r = \prod_n \left\{ \exp \left[-\frac{\Delta_{n,r}^2}{2} (1 - \exp[-i\nu_n t]) - \frac{i\nu_n t}{2} \right] \times (1 - \exp[-i\nu_n t])^{q_n} \frac{(-1)^{q_n} \Delta_{n,r}^{q_n}}{(2^{q_n} q_n!)^{1/2}} \right\} \quad (7)$$

where ϕ_f is the final vibrational level of the electronic ground state, which differs from the ground-state vibrational level (initial state in the Raman process) by q_n quanta in normal mode n . The intensity of the Raman transition $i \rightarrow f$ is then obtained from

$$I_{i \rightarrow f} \propto \nu_i \nu_s^3 |\alpha_{i \rightarrow f}|^2 \quad (8)$$

where ν_s is the energy of the scattered radiation.

For the alkyl(hydro)peroxo Cu(II) complexes, there are two CT transitions, π_{v}^* and π_{o}^* to Cu x^2-y^2 , and the Raman intensity is given by

$$I \propto |\alpha_1 + \alpha_2|^2 \quad (9)$$

where α_1 and α_2 represent the Raman polarizabilities of the π_{v}^* and $\pi_{\text{o}}^* \rightarrow \text{Cu } x^2-y^2$ CT transitions, respectively. The 536 and 756 cm⁻¹ vibrations were not included due to their very low intensities, leading to a four-mode (843, 809, 645, and 551 cm⁻¹ vibrations), two-state (π_{v}^* , $\pi_{\text{o}}^* \rightarrow \text{Cu } x^2-y^2$) analysis. The MCD results were also incorporated in the analysis by requiring that each simulated absorption band reproduce the relative intensity, peak maximum, and width of each of the Gaussian-resolved CT bands in Figure 3. This severely constrains the values of μ^2 , Δ , and E_0 . The directions of the dimensionless displacements, Δ , were obtained from the CT transition assignments and the nature of molecular orbitals involved in the transition. Both CT transitions promote electrons from peroxide-based antibonding orbitals to the Cu x^2-y^2 orbital, which has an antibonding interaction with the alkylperoxide. Thus, the bond length changes expected are $\Delta r_{\text{O}-\text{O}} < 0$ and $\Delta r_{\text{Cu}-\text{O}} > 0$. From the vibrational eigenvectors of each mode (Table 5), the signs for the Δ 's are $\Delta(\text{O}-\text{O}) < 0$, $\Delta(\text{O}-\text{C}) < 0$, $\Delta(\text{Cu}-\text{O}) > 0$, and $\Delta(\text{C}-\text{C}-\text{C}) > 0$. A direct modeling approach was then used to search for the complete parameter set that generates the best simultaneous fit to the experimental low-temperature solution absorption spectrum and solid rR profile data (Figure 7). The refined parameters are given in Table 8.

This analysis was also applied to the absorption and rR excitation profiles of L3CuOOH. The fitted parameters are summarized in Table 8, and the simulated absorption spectrum and rR excitation profiles are superimposed on the experimental data in Figure 8B,C.

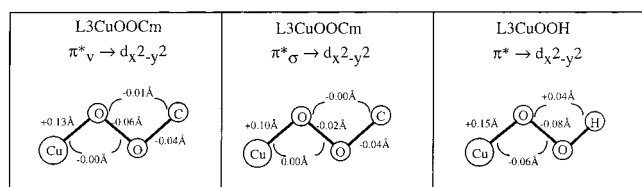
Table 8. Excited-State Parameters from Simultaneous Fit to the Absorption and Resonance Raman Data of L3CuOOCm and L3CuOOH

band	E_0 (cm ⁻¹)	Γ_r (cm ⁻¹)	$\Delta(\text{O}-\text{O})$	$\Delta(\text{O}-\text{C})$	$\Delta(\text{Cu}-\text{O})$	$\Delta(\text{C}-\text{C}-\text{C})$	μ_r^2
L3CuOOCm							
π^*_v	14 250	500	-1.09	-0.82	1.52	1.69	1.00
π^*_o	17 200	700	-0.50	-0.38	1.33	1.62	0.12
L3CuOOH							
π^*_v	14 150	500	-1.75		1.93		1.00
π^*_o	15 300	600	-1.65		1.83		0.41

Table 9. Comparison of Peroxide-to-Cu and Peroxide O-O Bonding

complex	$(C^M_{\pi^*})^2$ ratio ^a	$k_{\text{O}-\text{O}}$ (mdyn/Å) ^b	$\nu_{\text{O}-\text{O}}$ (cm ⁻¹)	$k_{\text{Cu}-\text{O}}$ (mdyn/Å) ^b	$\nu_{\text{Cu}-\text{O}}$ (cm ⁻¹)	$\pi^* \rightarrow x^2-y^2$ CT (cm ⁻¹)	ref
Cu end-on monomer	1.0	2.90 (2.86)	803	1.94 (1.89)	488	19 880 ^d	69
Cu end-on dimer	1.9	3.17 (3.10)	832	1.99 (1.94)	561	19 085 ^d	68
Cu side-on dimer	3.7	2.43 (2.43)	763	1.54 (1.42)	572	26 570 ^d	7
Cu ₂ OOH	<1.2	3.52 (3.70)	880	1.03 (1.20)	609	25 200 ^e	30
L3CuOOCm	1.1	3.22	843/809/756	3.03	645	16 590 ^e	g
L1CuOOCm	>0.8	<i>f</i>	844/802/755	<i>f</i>	652	17 460 ^e	g
L3CuOOCtBu	1.0	<i>f</i>	884/834/754	<i>f</i>	640	16 375 ^e	g
L3CuOOH	>0.3 ^c	3.51	843	2.94	624	16 560 ^e	g

^a $(C^M_{\pi^*})^2$ is the relative charge donation by peroxide (relative to end-on monomer). ^b Urey-Bradley force constants in parentheses. ^c Data complicated by the side-on dimer contamination and partial formation, see text. ^d $\pi^*_o \rightarrow \text{Cu } x^2-y^2$ CT transition. ^e $\pi^*_v \rightarrow \text{Cu } x^2-y^2$ CT transition. ^f NCA only performed for L3CuOOCm, and other alkylperoxo complexes are similar. ^g This work.

Scheme 2

The excited-state distortions can be expressed in terms of internal coordinates using the eigenvectors obtained from the NCA (Tables 5 and 7) and the calculated dimensionless displacements (Δ) from the above Raman analysis. The internal coordinate changes, Δr_i (Å), are related to normal coordinate displacements, Δ_n , by⁷⁰

$$\Delta r_i = 5.8065 \sum_n L_{i,n} \frac{\Delta_n}{\sqrt{\nu_n}} \quad (10)$$

in which $L_{i,n}$ is the i th element of the mass-weighted eigenvector, \mathbf{L}_n , for the n th normal mode. The schematic illustrations of the nuclear distortions of the Cu-O-O-C core of L3CuOOCm and the Cu-O-O-H core of L3CuOOH are shown in Scheme 2. They are given for both alkylperoxide π^*_v and $\pi^*_o \rightarrow \text{Cu } x^2-y^2$ CT excited states; however, for L3CuOOH the absorption and rR data do not resolve the two CT transitions, and thus the bond distortion estimates are averaged into one effective hydroperoxide $\pi^* \rightarrow \text{Cu } x^2-y^2$ excited-state distortion.

The major excited-state distortions are similar for both the alkyl- and hydroperoxo complexes and are along the Cu-O and O-O internal coordinates. The 0.13 Å (0.15 Å for L3CuOOH) Cu-O bond length change of the $\pi^*_v \rightarrow x^2-y^2$ CT transition of L3CuOOCm is quite large and reflects the strength of the π -bonding interaction between Cu x^2-y^2 and alkyl(hydro)peroxide π^*_v orbitals. The different distortions of alkylperoxo complexes in the two excited states reflect the observed differences in the rR profiles of the 843 and 809 cm⁻¹ vibrations relative to the 645 and 551 cm⁻¹ vibrations (Figure 7B,C). The rR intensities of the latter two vibrations arise from the Cu-O distortion. The $|\Delta r_{\text{Cu}-\text{O}}|/|\Delta r_{\text{O}-\text{O}}|$ ratio in Scheme 2

is larger in the $\pi^*_o \rightarrow \text{Cu } x^2-y^2$ than in the $\pi^*_v \rightarrow \text{Cu } x^2-y^2$ excited state, which thus leads to the resolved higher energy shoulder in the rR profiles in Figure 7C.

4. Alkyl(hydro)peroxide-to-Cu Donor Strength. In this section, the CT absorption intensities in Table 2 are used to obtain a quantitative experimental estimate of the donor strength of the alkyl(hydro)peroxide π^*_v and π^*_o orbitals. The CT transition intensity f directly reflects the amount of ligand character in the metal-based acceptor orbital involved in the CT transition. Using the formalism in ref 7,⁷ the contribution from the alkyl(hydro)peroxide π^* orbitals to the half-occupied Cu x^2-y^2 orbital is approximately given by

$$(C^d_{\pi^*})^2 = \kappa \frac{f}{\nu |\mathbf{r}|^2} \quad (11)$$

where κ is a constant (9.22×10^{-4} Å),⁴⁸ f is the oscillator strength, ν is the transition energy, and \mathbf{r} is the transition vector that coincides with the O-Cu bond.

This formalism has been applied to a series of Cu peroxide complexes, and the results are summarized in Table 9 for comparison.⁷ An approximately linear trend in donor strength has been observed on going from the Cu end-on monomer⁶⁹ to the Cu end-on (*trans*- μ -1,2) dimer⁶⁸ and the Cu side-on dimer,⁷ where the number of peroxide-to-Cu σ -bonds increases from one to two to four (Note: the donor strength is referenced to the end-on monomer which is set to 1.) Upon going from the end-on monomer to the μ -1,1-hydroperoxo dimer (Cu₂OOH), the donor strength per Cu-O bond dramatically decreases.³⁰ This decrease was ascribed to the polarization effect of protonation, which strongly stabilizes the peroxide-based molecular orbitals and increases the energy gap between the Cu d and the peroxide π^* orbitals. This stabilization is experimentally reflected in the peroxide π^* -to-Cu CT energies. The CT transition energy from the main Cu-bonding peroxide π^* orbital to the Cu x^2-y^2 orbital increases from 19 880 to 25 200 cm⁻¹ upon protonation for the same copper coordination number (Table 9). This larger energy gap results in a reduced bonding interaction and a decrease in the Cu-O bond strength (end-on monomer, $k_{\text{Cu}-\text{O}} = 1.94$ mdyn/Å; Cu₂OOH, $k_{\text{Cu}-\text{O}} = 1.03$ mdyn/Å).⁷²

In contrast, in this study the calculated donor strengths of the mononuclear alkylperoxides are much larger than the donor strength of the hydroperoxide in Cu_2OOH and are comparable to the peroxide in the end-on monomer (Table 9). This is due to the lower coordination number of the Cu in the alkyl(hydro)peroxo complexes (Cu_2OOH , five-coordinate; alkyl(hydro)peroxo complexes, four-coordinate), which decreases the energy of the Cu d manifold relative to that of Cu_2OOH (less repulsion and greater Z_{eff} of the Cu). Therefore, the alkylperoxide π^* and Cu d orbitals are close in energy, and the peroxide π^* -to-Cu(II) CT energy decreases from 25 200 cm^{-1} in Cu_2OOH to 16 600 cm^{-1} in L3CuOOCm . The resulting Cu–O bond becomes much stronger due to the increased charge donation (Table 9).

The hydroperoxo complex absorption data are complicated by the incomplete formation of this complex in solution as well as the presence of the side-on dimer (*vide supra*). However, on the basis of the similarity between the CT energies and the calculated Cu—O stretching force constants of the hydroperoxo and alkylperoxo complexes, the hydroperoxide is estimated to have a donor strength similar to that of the alkylperoxide.

5. Electronic Structure Calculations. In this section, electronic structure calculations performed on the alkyl(hydro)peroxo complexes are presented to complement experiments, which in turn evaluate the accuracy of the calculations. The calculations will then be extended to consider reactivity in the Discussion. Semiempirical INDO/S-CI calculations were performed on the symmetrized model $\text{Pz}_3\text{CuOOMe/Cs}$ as well as the original molecule in C_1 symmetry. On going from the C_1 to the C_s calculations, the CI state energies do not change, and there is a one-to-one correspondence for each excited state (Figure S7); therefore, only the results from the C_s symmetrized model are presented below.

Spin-unrestricted density functional calculations at the B3LYP level were then performed to obtain a description of the electronic structure of the alkylperoxo Cu(II) system. Parallel calculations were also performed on the hydroperoxo complex and similar results were obtained; therefore, only the results obtained for the alkylperoxo complex are presented here. The relevant part of the energy level diagram is shown in Figure 9. The orbitals are grouped into spin-up and spin-down sets; pure pyrazole ligand orbitals are excluded for clarity.

Cu(II) has nine d electrons, five spin-up and four spin-down. Due to the extra electron in the spin-up orbitals (Figure 9, left), these orbitals are stabilized in energy relative to their spin-down counterparts. This spin polarization is large enough to displace the spin-up d orbitals below the occupied peroxide spin-up π^*_{v} orbital. The hole in the Cu d manifold resides in the spin-down x^2-y^2 orbital and is high in energy due to its antibonding interaction with the alkylperoxide π^*_{v} orbital (Figure 9, right, $d_{x^2-y^2}-\pi^*_{\text{v}}$). Since all of the spin-up Cu d orbitals are occupied, the net bonding interaction and electronic excitations involve the spin-down set, which are the focus of this analysis. Energies and compositions of selected Cu/peroxide-based spin-down MOs (boxed in Figure 9) are given in Table 10, and the contours are shown in Figure 10.

5.1. Nature of the Cu–O–OR(H) Bond. When free peroxide forms a σ -bond to the alkylcarbon, its two degenerate highest energy occupied π^* orbitals split into two nondegenerate

(72) The normal coordinate analysis of Cu_2/O_2 complexes was previously performed using a Urey–Bradley force field. To have a direct comparison of force constants with the GVFF NCA results, the previous NCA results were transformed into generalized valence force constants using the corresponding matrix elements of the \mathbf{F} matrix generated by the Urey–Bradley force field.

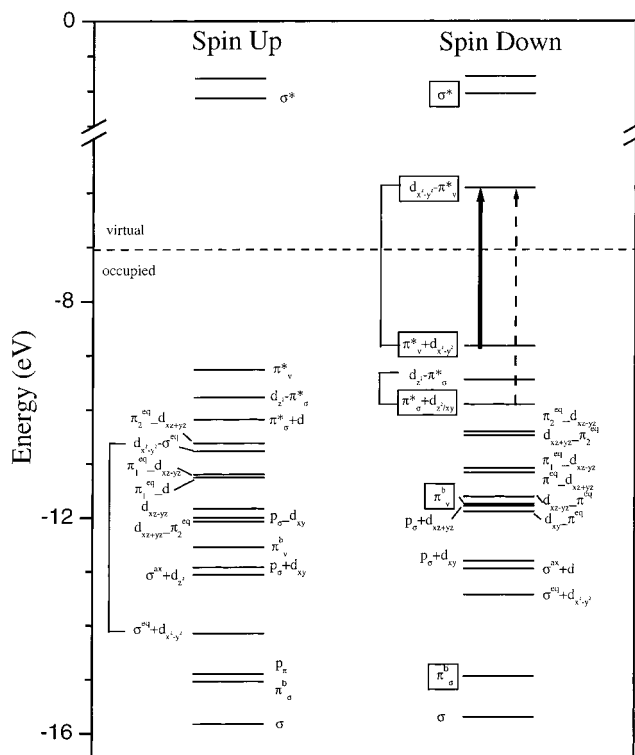


Figure 9. Energy level diagram obtained from a spin-unrestricted B3LYP calculation on the $\text{Pz}_3\text{CuOOMe/Cs}$ model. The orbitals are grouped into spin-up (left) and spin-down (right) parts. Individual orbitals are labeled according to their primary components in terms of fragment orbitals, and the first term in the label indicates the dominant nature of each molecular spin orbital. Each MO is described as a bonding (+) or antibonding (−) combination of the dominant two interacting fragment orbitals. (For pyrazole, the highest three occupied donor orbitals are labeled as π_2 , π_1 , and σ , respectively.) The corresponding bonding and antibonding combinations of the MOs are connected with brackets. When the interaction between fragment orbitals are mixed, the components are connected by “−” (e.g., the Cu x^2-y^2 -based MO, which has an antibonding interaction with alkylperoxide π^*_v orbital, is labeled as $d_{x^2-y^2}-\pi^*_v$). The Cu/peroxide-based MO labels are grouped in the center, and the Cu/pyrazole-based MO labels are grouped on the sides of the diagram. Labels: ax, axial pyrazole; eq, equatorial pyrazole ligand.

levels, designated π^*_{ν} and π^*_{σ} in Figure 9. The contours (Figure 10C,D and Table 10) indicate that both levels are involved in bonding interactions with the Cu d orbitals. The π^*_{ν} orbital lies perpendicular to the C_s plane of the molecule and has a strong π -interaction with the unoccupied spin-down Cu x^2-y^2 orbital (Figure 10D and 80a'' in Table 10). This results in a large splitting of the bonding and antibonding combinations of these fragment orbitals ($\sim 23\,560\text{ cm}^{-1}$, Figure 9). The π^*_{σ} orbital is in the C_s plane and has a σ -bonding interaction with the Cu xy/z^2 orbital (Figure 10C and 78a' in Table 10). Since both π^*_{σ} and Cu xy/z^2 are fully occupied, this does not contribute to the net bonding.⁷³

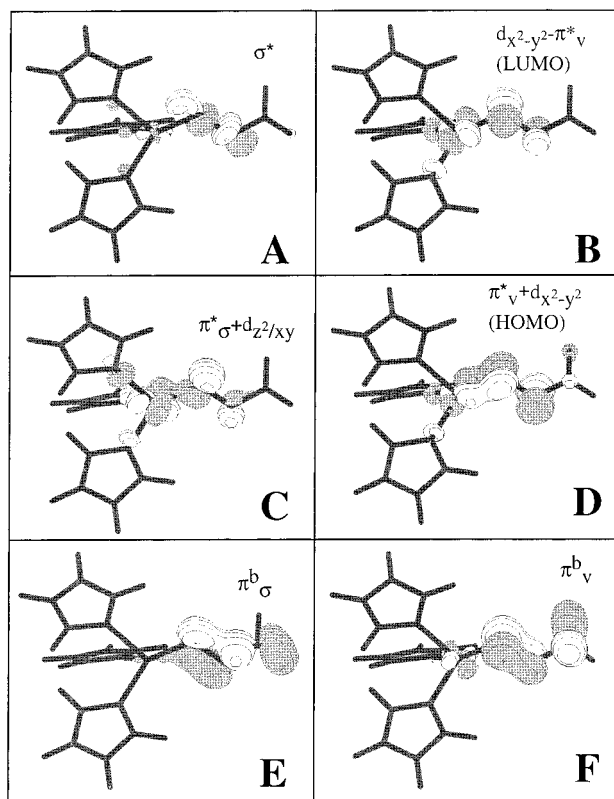
Significant changes also occur in other peroxide-based MOs upon bonding to the alkylcarbon and the Cu atoms. The two π^b orbitals of peroxide split in energy (designated π^b_v and π^b_σ in Figure 9) and are strongly polarized (Figure 10E,F and 58a', 70a'' in Table 10). π^b_σ is polarized toward the carbon atom and forms a σ -bond, while π^b_v is polarized toward the Cu. The splitting of π^b_v and π^b_σ is large ($\sim 25\,820\text{ cm}^{-1}$, Figure 9). This polarization effect has been analyzed by Root et al.³⁰ The net

(73) The π^*_σ orbital contains $\sim 4\%$ Cu 4s/4p character, which will contribute some net Cu–OOR bonding.

Table 10. Energies (eV) and Compositions (%) of Selected Spin-Down MOs, Spin Density Distributions, and Fragment Charges from B3LYP Calculation on Pz₃CuOOMe/Cs

level		energy	Cu%	Pz ^{ax} %	O% ^b	O% ^c	Me%	Pz ^{eq} % (×2)
σ^* ^a	86a'	-2.06349	2	19	25	17	6	15
$d_{x^2-y^2}-\pi^*_v$	81a''	-5.90283	41	1	30	11	3	7
$\pi^*_v + d_{x^2-y^2}$	80a''	-8.82458	21	1	22	38	7	6
$\pi^*_\sigma + d_{z^2/xy}$	78a'	-9.90490	37	10	25	7	1	10
π^*_v	70a''	-11.7379	10	0	33	21	25	5
π^*_σ	58a'	-14.9388	4	2	21	41	24	4
spin density			0.52	0	0.32	0.08	0	0.04
Mulliken charge			1.22	0.04	-0.48	-0.27	0.33	0.08
NPA ^d charge			1.33	0.03	-0.54	-0.28	0.34	0.07
ESP ^e fit charge			0.57	0.18	-0.32	-0.17	0.21	0.26

^a See ref 82. ^b Ligating oxygen atom. ^c Remote oxygen atom. ^d Natural population analysis. ^e Electrostatic potential.

**Figure 10.** Contour plots of selected spin-down MOs obtained from the B3LYP calculation on the Pz₃CuOOMe/Cs model. Contours are drawn at $\pm 0.06, 0.12, 0.18, 0.24, 0.30$, and $0.36 [e/\text{bohr}^3]^{1/2}$.

effect is a strengthened O—O bond, which is reflected experimentally in the large value of our NCA-derived O—O force constant, $k_{\text{O-O}} = 3.22 \text{ mdyne/\AA}$ for L3CuOOCm. The peroxide σ^* orbital is also very low in energy with respect to the free peroxide (Figure 9, top, and Figure 10A), resulting in the significant electrophilic character for the bound alkyl(hydro)peroxide. The implications for this low-lying alkyl(hydro)peroxide σ^* LUMO will be considered in the Discussion.

5.2. Comparison to Experiment. Our spectroscopic studies have defined the ground state of the alkylperoxo complexes as having a hole in the Cu x^2-y^2 orbital, with this orbital oriented such that its lobes are bisected by the Cu—OOR bond. The ground state was found to contain $\sim 62\%$ Cu character. The lowest unoccupied spin-down MO from B3LYP calculation is the Cu x^2-y^2 orbital, with its lobes bisected by the Cu—OOR bond (Figure 10B), consistent with experiments. The ground-state covalency can be obtained from the spin density distribution, which reflects the spatial distribution of the excess spin

($S = 1/2$).⁷⁴ The calculated spin density on the Cu atom is 0.52 (Table 10), which underestimates the Cu character and overestimates the covalency of the ground state.

The absorption, MCD, and rR data have shown that the main bonding interaction between Cu and the alkylperoxide is the π -interaction between the Cu x^2-y^2 and alkylperoxide π^*_v orbitals, which leads to a low-energy intense alkylperoxide $\pi^*_v \rightarrow \text{Cu } x^2-y^2$ CT band and a higher energy weak $\pi^*_\sigma \rightarrow \text{Cu } x^2-y^2$ CT band. The calculation reproduces the dominant bonding interaction between Cu and the alkylperoxide (Figure 10B,D) and predicts the intense CT transition from the alkylperoxide π^*_v to the Cu x^2-y^2 orbital due to the strong overlap of these two interacting orbitals (Figure 9, solid thick arrow). The CT oscillator strength f is estimated to be ~ 0.25 ,⁵⁰ significantly larger than the experimentally observed value (~ 0.08 , Table 2), reflecting the over-covalent Cu—O bond. The π^*_σ -to-Cu x^2-y^2 CT transition is predicted to have higher energy with almost no intensity due to the poor overlap between the interacting orbitals (Figure 9, broken arrow). The calculated π^*_v/π^*_σ splitting is 8710 cm^{-1} , significantly larger than the experimentally observed $\sim 2575 \text{ cm}^{-1}$ value (Table 2, Figure 3).

The experimentally observed Cu d orbital energy order is $x^2-y^2 > z^2 > xy > xz+yz > xz-yz$, and all d—d transitions are to lower energy than the CT bands. The calculated Cu d orbital energy ordering generally agrees with experiment, but the calculated Cu xy orbital is too low (Figure 9). The predicted d—d transitions overlap with the ligand-to-metal CT bands, which reflects the fact that the B3LYP-calculated Cu d manifold is too low in energy relative to the ligand valence orbitals. This results in the highly mixed MOs (Figure 9) and also correlates with the overestimate of the calculated ground-state covalency.

Thus, the B3LYP calculation predicts the correct electronic ground state and main bonding interactions between the Cu atom and the alkylperoxide ligand. However, the calculated Cu d manifold is too low in energy, which results in the overlap of the ligand field and CT manifolds and a *too covalent* Cu—OOR(H) bond.

Discussion

This study has allowed us to develop a detailed description of the electronic structures of the four-coordinate mononuclear end-on alkyl- and hydroperoxo Cu(II) complexes using a combination of spectroscopic methods. The dominant bonding interaction between the Cu(II) atom and the alkyl(hydro)peroxide is the π -donor interaction of the alkyl(hydro)peroxide π^*_v orbital with the Cu x^2-y^2 orbital, whose lobes are bisected by the Cu—OOR(H) bond, producing the low-energy intense

(74) The MO decompositions of Table 10 were calculated from the squares of the coefficients of the atomic orbitals of the normalized MOs assuming no overlap.

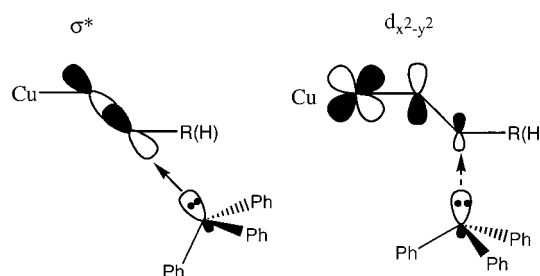
$\pi^*_v \rightarrow \text{Cu } x^2-y^2$ CT transition. The observed Cu–O bond is strong, and the alkyl(hydro)peroxide is a surprisingly strong donor. This strong Cu–OOR(H) bonding interaction results from the low coordination number of the Cu atom (CN = 4) and the distorted T_d site symmetry, both of which increase the effective nuclear charge on the Cu and reduce the repulsive interaction with the ligands. The Cu d manifold is greatly stabilized relative to a five-coordinate species, and the energy separation from the alkyl(hydro)peroxide π^* orbitals is greatly reduced. This strengthens the Cu–OOR(H) interaction and results in the observed large peroxide-to-Cu charge donation and the increased Cu–O stretching force constant.

The O–O bond was found to be strong, which is similar to what was observed in the five-coordinate μ -1,1-bridged Cu_2OOH . This indicates that the strengthened O–O bond is determined by the polarization effect of the alkylcarbon(proton) and is not affected much by the alkyl(hydro)peroxide-to-Cu charge donation. The difference in the O–O vibrational frequency between L3CuOOH and Cu_2OOH arises from the larger mechanical coupling between the Cu–O and O–O vibrations in Cu_2OOH due to its larger Cu–O–O angle. The alkylcarbon(proton) polarization effect could make a significant contribution to the reactivity of these complexes, as this lowers the energy of the unoccupied σ^* orbital, rendering the complex rather electrophilic. In the four-coordinate complexes, the significant charge donation from the alkyl(hydro)peroxide to Cu(II) further contributes to this electrophilicity. As a result, electrophilic attack of a substrate or direct H atom abstraction are both possible reaction pathways involving the low-lying alkyl(hydro)peroxide σ^* orbital.

The experimental reactivity of L1CuOOR has been reported.²⁶ This complex undergoes bimolecular electrophilic oxo transfer to PPh_3 , forming OPPh_3 (78% yield). A unimolecular decomposition reaction with solvent pentane resulted in *tert*- $\text{BuOOC}_5\text{H}_{11}$ (20%) and *tert*- BuOH (59%) products. This reaction was proposed to occur via a classical radical reaction initiated by tBuOO^\bullet or tBuO^\bullet , with tBuOO^\bullet favored as the reaction initiator. Bimolecular one-electron oxidation of phenol yields the phenol radical (228%) and coupling products. While similar in its reactivity with PPh_3 and phenol to L1CuOOR , the hydroperoxo complex with the L3 ligand does not react with pentane solvent. However, the synthetic precursor L3CuOH was observed as one product,⁷⁵ which probably reflects the well-established Cu(II)-catalyzed disproportionation of the coordinated hydroperoxide.^{76,77}

In this study, the B3LYP electronic structure calculations have been evaluated and calibrated by our spectroscopic results, and these calculations allow further consideration of the reactivities of these alkyl(hydro)peroxo Cu(II) complexes. In addition, frontier molecular orbital (FMO) theory, which has been used to examine the reactivity of the planar side-on and bis-(μ -oxo) Cu_2/O_2 cores toward electrophilic aromatic substitution reactions,^{78–80} can be extended further to the oxo-transfer reaction. In the oxo-transfer reaction, the alkyl(hydro)peroxo complex

Scheme 3



acts as an electrophile. PPh_3 has a lone electron pair in an sp^3 hybrid donor orbital, which favors a σ -type interaction. In FMO theory,⁸¹ the lowest unoccupied molecular orbital on the electrophile and the highest occupied donor orbital on the nucleophile participate in the reaction. The atomic charge, energy splitting, symmetry, and orbital coefficients of these interacting FMOs are important factors that direct the reaction. From Table 10, the total charge decomposition indicates that the remote O atom has much less negative charge than the ligating O atom and is thus favored for electrophilic attack. The bulky nature of the PPh_3 substrate and the steric hindrance of the trispyrazolylborate ligand also favor the attack at the remote O atom. Experimentally, the μ -1,1-bridged complex Cu_2OOH is more efficient than L1CuOOR and L3CuOOH at oxo transfer, which is consistent with the increased steric constraint of the trispyrazolylborate ligand.

The lowest unoccupied peroxide-based MO of the alkyl(hydro)peroxo complex is the σ^* orbital, which favors an end-on σ -type interaction with the donor orbital (Figure 10A and Scheme 3 left). The half-occupied Cu x^2-y^2 orbital also has some peroxide π^*_v contribution and has π -symmetry, which would require a pseudo- σ interaction from the side with the lone pair of PPh_3 (Figure 10B and Scheme 3, right). Both of these orbitals can act as acceptors in this reaction. Although the energy separation relative to the lone-pair donor orbital of PPh_3 favors the Cu x^2-y^2 orbital as the acceptor, the MO coefficient of the remote O atom argues in favor of the σ^* orbital, which is highly localized on the O–O moiety (Figure 10A and Table 10).⁸² To differentiate their contributions to reactivity, calculations were performed where an exogenous H atom was introduced as an electrophilic mechanistic probe and allowed to freely move around the peroxide moiety in the hydroperoxo complex. The results show that the reaction coordinate along the O–O bond is energetically favored in an end-on attack by the H atom.⁸³ Therefore, the oxo-transfer to PPh_3 reaction likely occurs through the σ^* pathway (Scheme 3, left).

We can further use the experimentally calibrated B3LYP calculations to evaluate the energetics of the possible mechanistic pathways of the alkyl(hydro)peroxo complexes involving O–O and Cu–O bond cleavage and H atom abstraction (Scheme 4). In heme enzymes, heterolytic cleavage of an O–O bond to generate a high-valent Fe-oxo species has been proposed and is a generally accepted step in the reaction pathway in the

(75) Fujisawa, K., unpublished results.

(76) Thompson, J. S. In *Biological and Inorganic Copper Chemistry*; Karlin, K. D., Zubieta, J., Eds.; Adenine: Gunderland, NY, 1986; Vol. 2, p 1.

(77) Zuberbuhler, A. D. In *Copper Coordination Chemistry: Biochemical and Inorganic Perspectives*; Karlin, K. D., Zubieta, J., Eds.; Adenine: Gunderland, NY, 1983; p 237.

(78) Pidcock, E.; Obias, H. V.; Zhang, C. X.; Karlin, K. D.; Solomon, E. I. *J. Am. Chem. Soc.* **1998**, *120*, 7841.

(79) Pidcock, E.; Obias, H. V.; Abe, M.; Liang, H.-C.; Karlin, K. D.; Solomon, E. I. *J. Am. Chem. Soc.* **1999**, *121*, 1299.

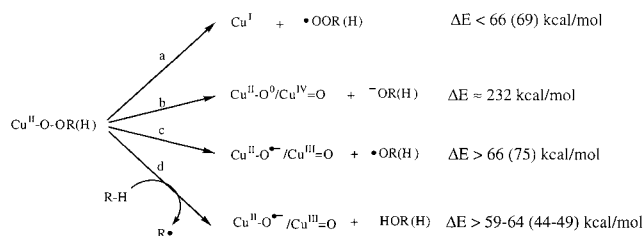
(80) Pidcock, E.; DeBeer, S.; Obias, H. V.; Hedman, B.; Hodgson, K. O.; Karlin, K. D.; Solomon, E. I. *J. Am. Chem. Soc.* **1999**, *121*, 1870.

(81) Fleming, I. *Frontier Orbitals and Organic Chemical Reactions*; John Wiley & Sons: New York, 1976.

(82) The σ^* orbital has a large contribution from the outer-shell 9s basis function of Cu and is an artifact of the large basis set used in the calculation. This is excluded in the MO decomposition analysis.

(83) Both triplet and singlet calculations were performed, where the end-on and side-on attacks take place, respectively. The end-on attack pathway is ~ 30 kcal/mol lower in energy than the side-on attack.

Scheme 4



P450 system.⁸⁴ The energetics were calculated to be highly favorable.⁸⁵ Conversely, the heterolytic cleavage of an O—O bond to generate a formally Cu^{IV}-oxo species (Scheme 4b) is extremely unfavorable, with $\Delta E \approx 232$ kcal/mol. The ΔE of the homolytic cleavage of an O—O bond (Scheme 4c) (to generate a formally Cu^{III}-oxo species and the $\bullet\text{OR}(\text{H})$ radical) is calculated to be 66 kcal/mol (75 kcal/mol for the hydroperoxo complex), also not a favorable pathway. The direct H atom abstraction pathway generates the same formally Cu^{III}-oxo intermediate as in the homolytic O—O cleavage, while forming an O—H bond by breaking a C—H bond (Scheme 4d). The bond energy difference of O—H and C—H bonds somewhat stabilizes this reaction, and the ΔE is estimated to be around 59–64 kcal/mol for the alkylperoxo complexes (44–49 kcal/mol for the hydroperoxo complex, as this generates H₂O). The ΔE of the reductive cleavage of the Cu—O bond (Scheme 4a) is calculated to be comparable to that of the homolytic cleavage of the O—O bond, about 66 kcal/mol (69 kcal/mol for the hydroperoxo complex). All calculated reaction pathways are uphill in terms of the total energy and therefore unfavorable. On the basis of the standard entropy values of similar reactants and products,⁸⁶ the entropy change is estimated to contribute ~ 5 –10 kcal/mol to the reactions. Usually the magnitude of solvation energy of polar molecules in water is less than -15 kcal/mol and no more than -30 kcal/mol for charged molecules.^{87,88} The reactions considered here were all studied in the nonpolar solvent pentane, and thus the solvation contribution is not large.

Compared to the spectroscopic results, the B3LYP calculations of the alkyl(hydro)peroxo complex overestimate the covalency of the Cu—O bond (52% Cu character from calculations, 62% Cu character from experiments). The Cu—O bond energy is inversely proportional to the Cu character in the antibonding combination MO. Therefore, the energy of the Cu—O bond, which is just the energy change of the reductive homolytic cleavage of the Cu—O bond (Scheme 4a), is significantly overestimated, and the actual ΔE for this reaction should be reduced and less unfavorable. This is consistent with the experimentally observed tBuOO \bullet reactivity. The fact that the homolytic cleavage of the Cu—O bond occurs for the *tert*-butylperoxide complex but not for L3CuOOH can be accounted

(84) Solomon, E. I.; Brunold, T. C.; Davis, M. I.; Kemsley, J. N.; Lee, S.-K.; Lehnert, N.; Neese, F.; Skulan, A. J.; Yang, Y.-S.; Zhou, J. *Chem. Rev.* **2000**, *1*, 235.

(85) Harris, D. L.; Loew, G. H. *J. Am. Chem. Soc.* **1998**, *120*, 8941.

(86) Considering the bulky nature of the trispyrazolylborate ligand, the entropy values of all the intermediate Cu complexes were approximated to be equivalent to the original alkyl(hydroperoxo) complex. tBuOO \bullet and tBuO \bullet were approximated as tBuOH, and HOO \bullet and HO \bullet as HOOH and HOH, respectively. Standard values were taken from the following: *CRC Handbook of Chemistry and Physics*, 76th ed.; Lide, D. R., Ed.; CRC Press: Boca Raton, 1995.

(87) Tomasi, J.; Persico, M. *Chem. Rev.* **1994**, *94*, 2027.

(88) Cramer, C. J.; Truhlar, D. G. In *Quantitative Treatment of Solute/Solvent Interactions*; Politzer, P., Murray, J. S., Eds.; Elsevier: Amsterdam, 1994; Vol. 1, pp 9–54.

Table 11. Comparison of Calculated Properties of Cu^{II}OOH, Intermediate Generated by Homolytic O—O Cleavage and Cu^{II} Oxide Analogue

Q^a	Cu	Pz ^{ax}	O	OH	Pz ^{eq} \times 2	BH
Cu ^{II} OOH	1.20	−0.41	−0.51	0	−0.37	0.44
intermediate	1.25	−0.40	−0.64		−0.33	0.44
Cu ^{II} oxide	0.79	−0.45	−0.83		−0.45	0.38
r (Å)	$r(\text{Cu—O})$		$r(\text{Cu—Pz}^{ax})$		$r(\text{Cu—Pz}^{eq})$	
Cu ^{II} OOH	1.776		2.285		2.009	
intermediate	1.665		2.332		1.945	
Cu ^{II} oxide	1.743		2.443		2.193	

^a Mulliken charge.

for by the relative stabilities of the tBuOO \bullet and HOO \bullet radical products; the former is stabilized by hyperconjugation.⁸⁹

In contrast to the Cu—O bond, in Scheme 4b, c, and d, the O—O bond strength is mainly determined by the alkylcarbon (proton) and is thus not significantly affected by the overly covalent Cu—O bond. The ΔE of homolytic O—O cleavage and direct H atom abstraction are high due to the species generated, formally a Cu^{III}-oxo or Cu^{II}-oxyl intermediate. The calculated atomic charges and the optimized bond lengths of this intermediate are summarized in Table 11, along with the values of the hydroperoxo Cu(II) complex (Cu^{II}OOH) and the Cu^{II} oxide analogue. The charge on the oxygen atom of this intermediate is close to that of the original Cu^{II}-OOH complex, and thus it is approximately a Cu^{II}-oxyl species. The increased negative charge on the ligating oxygen relative to that of the hydroperoxo complex mainly comes from the equatorial pyrazole ligands that are partially oxidized in the formation of this Cu^{II}-oxyl intermediate. Pyrazole is, however, difficult to oxidize, and combined with the high Cu^{II}/Cu^{III} redox potential, this intermediate is at high energy. The optimized Cu—O bond decreases by ~ 0.11 Å in the Cu^{II}-oxyl species. From Badger's rule, this bond length change corresponds to an $\sim 53\%$ increase in bond strength. Since the B3LYP electronic structure calculations overestimate the Cu—O bond strength (vide supra), which will stabilize the Cu^{II}-oxyl intermediate formed, the total energy changes of the homolytic O—O cleavage reaction pathways (Scheme 4c,d) should be higher than predicted and the reactions more unfavorable. Thus, the phenol coupling reaction that occurs in these alkyl(hydro)peroxo complexes likely does not occur through H atom abstraction, but through one-electron oxidation and deprotonation. This is consistent with the fact that a variety of Cu(II) complexes catalyze the phenol coupling reaction.^{90–92} In contrast, in non-heme iron systems, H atom abstraction and cleavage of the O—O bond of an Fe^{III}-OOH species to generate an Fe^{IV}-oxo intermediate is calculated to be a favorable pathway, with ΔE close to zero.⁹³ This is consistent with the low Fe^{III}/Fe^{IV}-oxo redox potential relative to that of Cu^{II}/Cu^{III}, which stabilizes the Fe^{IV}-oxo intermediate.

In dopamine β -monooxygenase (D β M) and peptidylglycine hydroxylating monooxygenase (PHM), a Cu^{II}OOH species is generally proposed as a mechanistic intermediate which performs H atom abstraction from the substrate, resulting in a high-energy Cu^{II}-oxyl/Cu^{III}-oxo species.¹ Water is a product in this

(89) Similar reactivity is also not observed for the Cu₂OOH complex, which is likely related to the higher coordination number of the Cu atom, which lowers its redox potential, and the fact that two Cu—O bonds would cleave.

(90) Baesjou, P. J.; Driessen, W. L.; Challa, G.; Reedijk, J. *J. Mol. Catal. A* **1998**, *135*, 273.

(91) Baesjou, P. J.; Driessen, W. L.; Challa, G.; Reedijk, J. *Macromolecules* **1999**, *32*, 270.

(92) Feringa, B.; Wynberg, H. *Tetrahedron Lett.* **1977**, *50*, 4447.

(93) Neese, F.; Solomon, E. I., submitted for publication.

reaction, which is favored in an aqueous environment. (The active sites in the enzymes are highly solvent accessible.^{21,22}) The Cu ligand environment is also different in the proteins relative to that of the alkyl(hydro)peroxo complexes studied here. The crystal structure of PHM shows that the Cu_B center, where substrate hydroxylation occurs, has a methionine ligand in this four-coordinate distorted T_d site.^{21,22} The mechanistic role of the sulfur ligand is not clear, and whether this feature can contribute to the stabilization of a high-energy Cu^{II}-oxyl/Cu^{III}-oxo species is still an open question. Parallel studies on the enzymes in comparison to these model studies should provide insight into whether the ligand environment lowers the energy of the Cu^{II}-oxyl/Cu^{III}-oxo intermediate such that this pathway of enzymatic catalysis can occur (Scheme 4d). In addition to hydroxylation, electrophilic sulfoxidation⁹⁴ and epoxidation reactions⁹⁵ are observed for D β M and can be considered to occur via oxo-transfer reaction (Scheme 3, left).

Summary

This study developed an experimental and theoretical electronic structure description of four-coordinate mononuclear alkyl(hydro)peroxo Cu(II) complexes and evaluated how this electronic structure contributes to reactivity. The main bonding interaction between Cu(II) and the alkyl(hydro)peroxide is the π -donor interaction of the alkyl(hydro)peroxide π^*_v orbital to the Cu x^2-y^2 orbital, which dominates the observed spectroscopic features. The alkyl(hydro)peroxide is a surprisingly strong donor in these complexes relative to the hydroperoxide ligand of the μ -1,1-bridged complex Cu₂OOH.³⁰ This derives from the low coordination number of the Cu and its distorted T_d site

(94) May, S. W.; Phillips, R. S. *J. Am. Chem. Soc.* **1980**, *102*, 5981.

(95) Padgett, S. R.; Wimalasena, K.; Herman, H. H.; Sirimanne, S. R.; May, S. W. *Biochemistry* **1985**, *24*, 5826.

symmetry, both of which increase the effective nuclear charge on the Cu and result in an increased donor interaction, leading to the strong Cu–O bond. The alkylation(protonation) polarizes the alkyl(hydro)peroxide-based MOs and strengthens the O–O bond. The unoccupied σ^* orbital is greatly lowered in energy due to bonding of the R(H) group to the peroxide, resulting in activation of the complexes for electrophilic attack. The H atom abstraction and homolytic O–O cleavage reactions are found to be highly unfavorable due to the high energy of the Cu^{II}-oxyl intermediate that would be generated in these alkyl(hydro)peroxo Cu(II) complexes. These studies provide the foundation for understanding the enzymatic reactivities in the noncoupled binuclear copper enzymes D β M and PHM.

Acknowledgment. This research is supported by NIH Grant DK-31450 (E.I.S.). P.C. is a Stanford Graduate Fellow. K.F. thanks NEDO for the financial support of the project on Technology for Novel High-Functional Materials (AIST). Dr. Nicolai Lehnert is acknowledged for insightful discussions on the vibrational properties of the alkylperoxo complexes and Dr. Elna Pidcock and Mark Henson for collecting preliminary resonance Raman data.

Supporting Information Available: Complete NCA force fields and model coordinates of N₃CuOOCCH₃ and N₃CuOOH, INDO/S-CI calculation results (CI state energy level, MO contours plots, excited-state natural orbital analysis), coordinates for all DFT calculations, absorption, rR, and excitation profiles of L1CuOOCm, L3CuOOCm and L3CuOOtBu, and energy level and MO contours for BPz₃CuOOH/Cs DFT calculations (PDF). This material is available free of charge via the Internet at <http://pubs.acs.org>.

JA0016755